*minerals*

MDPI

*Article*

# Ore-Bearing Magmatic Systems with Complex Sn–Au–Ag Mineralization in the North-Eastern Verkhoyansk–Kolyma Orogenic Belt, Russia

**Vera A. Trunilina * and Andrei V. Prokopiev**

Diamond and Precious Metal Geology Institute, Siberian Branch, Russian Academy of Sciences, Lenin Av. 39, 677980 Yakutsk, Russia; prokopiev@diamond.ysn.ru

* Correspondence: v.a.trunilina@diamond.ysn.ru; Tel.: +7-914-101-6992

**Abstract:** This paper reports the results of a study of magmatic rocks with Sn–W–Au–Ag mineralization from the Kuranakh, Elikchan, and Istekh ore fields in the Northern batholith belt of the north-eastern Verkhoyansk–Kolyma orogenic belt in Eastern Russia. Using petrographic, mineralogical, geochemical, and isotopic methods, we determined the mineral compositions, petrochemistry, and geochemistry of magmatic rocks, the P–T conditions of their generation and crystallization, and their geodynamic affinity. The studied magmatic rocks have common geochemical characteristics that likely reflect the influence of fluids supplied from a long-lived, deep-seated mantle source. The ore fields are characterized by Sn–W–Au–Ag–Pb polygenetic mineralization. The magmatic and metallogenic evolution comprised five stages for the formation of magmatic rocks and ores. During the first stage (Berriasian–Barremian), arc-related magmatic rocks formed in an active continental margin setting and were associated with Au–Ag mineralization. The second, third, and fourth stages (Aptian–Campanian) took place in a crustal extension and rift setting, and were accompanied by Au–Ag and Sn–W mineralization. During the fifth (post-magmatic) stage, Sn–Ag–Sb and Pb–Ag mineralization occurred.

**Keywords:** petrography; mineralogy and geochemistry of magmatic rocks; ore mineralization; Verkhoyansk–Kolyma orogenic belt



**Citation:** Trunilina, V.A.; Prokopiev, A.V. Ore-Bearing Magmatic Systems with Complex Sn–Au–Ag Mineralization in the North-Eastern Verkhoyansk–Kolyma Orogenic Belt, Russia. *Minerals* **2021**, *11*, 266. https://doi.org/10.3390/min11030266

Academic Editors: Fernando Noronha and Jaroslav Dostal

Received: 16 January 2021
Accepted: 1 March 2021
Published: 4 March 2021



## 1. Introduction

In the northern Verkhoyansk–Kolyma orogenic belt (NE Asia), two major metallogenic belts are recognized: the Yana-Kolyma and North-Verkhoyansk. Their principal metals are tin and gold [1,2] (Figure 1). The largest high-tonnage Sn deposits are concentrated in the north-eastern part of the orogenic belt, including those of Deputatskoye, Churpunya, Polyarnoye, and Odinokoye (North-Verkhoyansk metallogenic belt). Many of these deposits have complex metallogenic characteristics, with Sn most commonly accompanied by W, Pb, Zn, Bi, Sb, and less commonly, Ag and Au. Such deposits are known in Alaska, Erzgebirge (Germany), Spain, Kazakhstan, Australia, and Bolivia, where tin mineralization occurs in association with Au, W, Bi, As, and Sb [3]. The origin of the deposits is generally associated with the emplacement of granitoids. Flerov [4] identified the following stanniferous formations in the Verkhoyansk–Kolyma orogenic belt: batholith-like granites with associated cassiterite–quartz, greisen and skarn deposits, as well as Sn-bearing pegmatite deposits; diorite–granodiorite–granites with cassiterite–silicate–sulphide and Sn–polymetallic deposits; and subvolcanic granites with greisen and cassiterite–silicate mineralization. In addition to these, Mitrofanov [5] recognized a tin porphyry formation associated with subvolcanic intrusions accompanied by explosive breccias. However, despite various studies of tin metallogeny, there is no consensus regarding the genesis of parental granitoid melts, the evolution of these melts, and the sources of metals. The granitoids are considered to have been derived from crustal, mantle, and crustal–mantle

melts [6–11]. The polygenetic nature of the ore–magmatic systems, that is, their formation as a result of the existence of magma chambers at different depths, is an important indicator of their high levels of mineralization [12,13]. High Sn content and the presence of cassiterite, native tin, and its intermetallic compounds in basaltic melt derivatives have been noted by many studies [14–18]. Thus, the available data allow the consideration of deep-level melts as one of the possible sources of tin and associated metals. According to Efremov [19], the metallogenic profile of granitoids is controlled mainly by the composition of magma chambers in the metasomatized mantle, whereas the formation of tin-bearing granitoids is related to the mixing of deep-seated melts and continental crust material. However, most researchers have identified crustal strata as the main source of tin, and consider that tin-bearing magmatic complexes form by the interaction of mantle and upper-crustal melts, although mantle-level heat flows and fluids initiate magma generation in the crust, leading to the fractionation of ores [20–22].

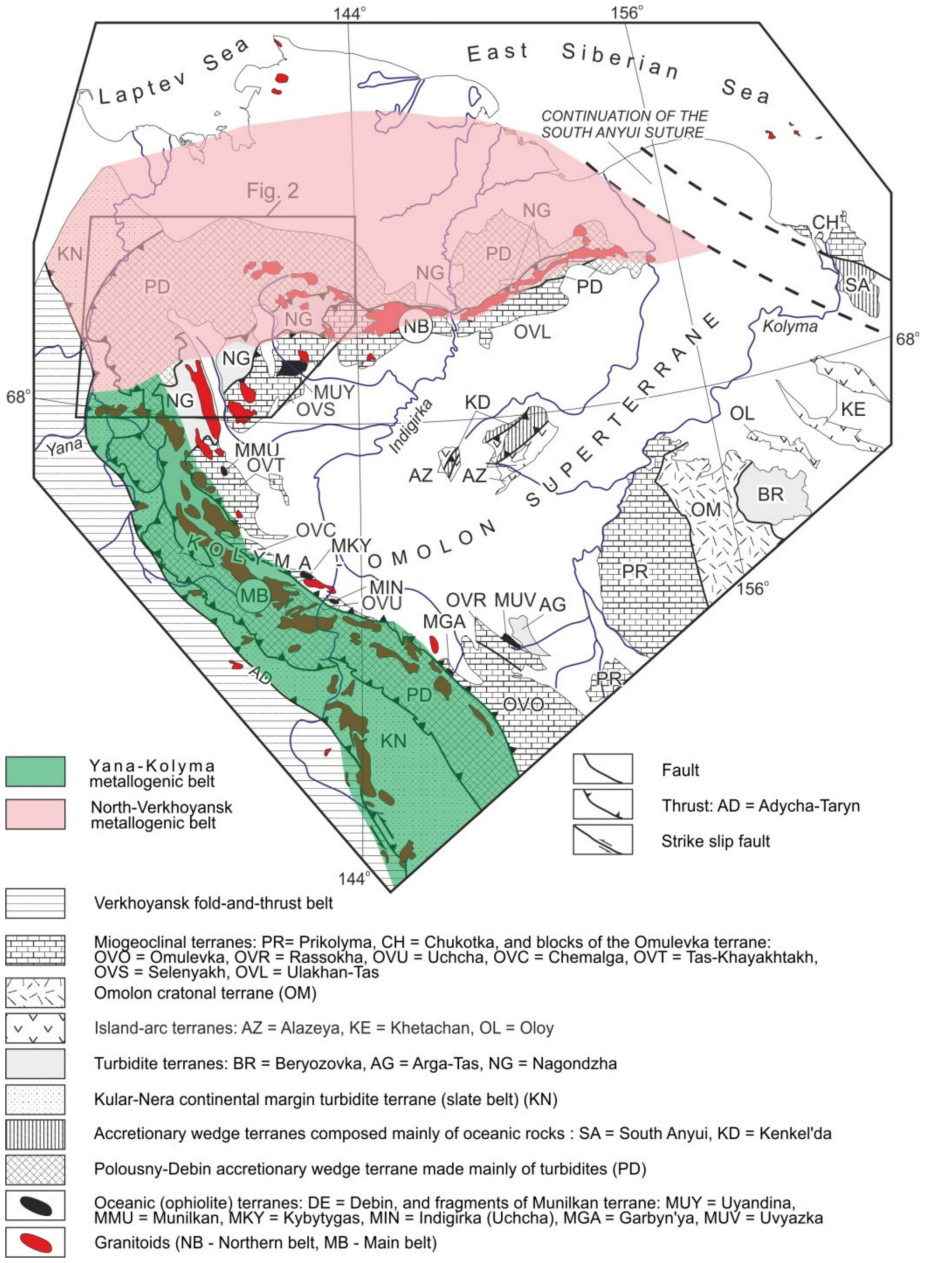


**Figure 1.** Tectonic map of the north-eastern Verkhoyansk–Kolyma orogenic belt, modified from [1,2].

Primary gold deposits can be subdivided into orogenic, epithermal, and intrusion-related deposits [23–25]. Goryachev and Pirajno [26] proposed an expansion of this classification by adding detailed systematics of Phanerozoic orogenic gold mineralization, in accordance with the mineralogical–geochemical features of the ores. Goryachev [27] recognized three types of orogenic gold mineralization in the Verkhoyansk–Kolyma orogenic belt: Au–sulphide, veinlet-disseminated; Au–quartz, veined; and Au–Bi (gold–rare-metal). All types of deposits and occurrences are hosted in Permian–Jurassic clastic rocks within and near granitoid plutons. A somewhat different classification has been proposed by Khanchuk [28]: Au–Ag–quartz deposits associated with intrusions of various compositions; Au–rare-metal deposits accompanying granodiorite and granite intrusions; and Au–sulphide mineralization spatially associated with monzonite and granite intrusions. Au–Ag epithermal deposits are associated with volcanic rocks and subvolcanic plutons of andesite–rhyolite composition.

Current explanations for the genesis of gold mineralization are as diverse as those for tin deposits, including from largely crustal [29] to largely mantle (for a number of Au–Hg–Sb and Ag–Sb deposits) [30] origins, to the currently favored mantle–crustal genesis [31,32]. Borisenko et al. [33] concluded that the formation of large Au–sulphide deposits in North Asia involved multiple stages of ore-deposition, magmatism, and polygenetic source rocks for the ore materials, as in the case of large Sn deposits. The sources of the melts were reworked crustal substrata and juvenile material, which served to enrich the crust with gold [25].

The aim of this study was to obtain new information about the genesis of complex tin deposits and associated gold mineralization in the north-eastern Verkhoyansk–Kolyma orogenic belt, by investigating the structurally complex ore fields of Kuranakh, Elikchan, and Istekh as case studies.

## 2. Methods

We established the internal structure of magmatic rock units, their relationship with one another, and their relationship with ore bodies. All types of magmatic rocks and ore zones present in the studied deposits were sampled for analytical investigation (more than 200 samples were sampled). The petrography of granitoid massifs and dykes in the ore fields was studied using an Olympus optical microscope (Leica, Germany), allowing conclusions to be drawn regarding the crystallization and evolutionary paths of the contributing melts.

The composition of rock-forming and accessory minerals was studied using the Camebax-micro x-ray microanalyzer (Cameca, Courbevoie, France) and a Jeol JSM-6480LV scanning microscope (JEOL, Tokyo, Japan).

Complete whole-rock geochemical analyses and quantitative spectral and inductively coupled plasma–mass spectrometry (ICP–MS) analyses of element contents in ores were performed, followed by mathematical processing of the data using the CGDkit, Igpet, and PetroExplorer software [34–36]. On this basis, we determined the generation and crystallization conditions of the melts and identified potential ore-bearing units.

Feldspars were studied using optical methods with a Fedorov universal stage (the Fedorov method) [37], allowing the determination of zoning patterns and structural ordering of minerals. The Fedorov method involves determining the shape and orientation of the optical indicatrix in a crystal. The degree of structural (or crystal) ordering (SO) is defined as the amount of deviation of the real (observed) spatial lattice of a crystal from the ideal (theoretical) spatial lattice, with this deviation decreasing with increasing temperature [38,39].

All analyses, with the exception of ICP–MS, were conducted at the Diamond and Precious Metal Geology Institute (DPMGI) of the Siberian Branch of the Russian Academy of Sciences, Yakutsk, Russia. Chemical compositions of the rocks were determined using conventional wet-chemistry analytical techniques.

Trace elements were detected using a PGS-2 spectrograph equipped with a multichannel atomic emission spectral analyzer from BMK Optoelectronics, Russia. The sample mixed with a refractory buffer is vaporized from the carbon electrode channel filled with an internal reference. The buffer for the atomic emission analysis of volatile elements is a mixture of 7 weight fractions of $Al_2O_3$, 3 fractions of $CaCO_3$, and 1 fraction of $K_2CO_3$ and 0.02% $Bi_2O_3$. The buffer for carbonates consists of 5 weight fractions of $Al_2O_3$, 4 fractions of $SiO_2$, and 1 fraction of $K_2CO_3$ and 0.02% $Bi_2O_3$. It was prepared in the same way as for silicates. Standards and samples were diluted with a buffer in the optimal weight ratio of 1:2. The buffer for elements of the iron group was 0.05% of the internal standard mixed with carbon powder. The carbon powder ensures uniform evaporation of the sample. The weight ratio of the buffer to the sample was 1:1. Based on the results of burning standards, diagrams were constructed which help to determine the content of the analyzed elements. To correct variations in the position of the spectrum, we used reference lines (Pd 302.79 Nm and 342 Nm). The chemical composition and characteristics of minerals and rocks in the studied samples are given in Tables S1–S5 [40–52].

The determination of Au and Ag content in the rocks was performed by the atomic absorption method on the 3500 device of Thermo Fisher Scientific, USA. The accuracy of Au and Ag detection was 0.002 ppm and 0.005 ppm, respectively, while the reproducibility correspondsed to an RSD (relative standard deviation) value 1 $\pm$ 0.3% and 5 $\pm$ 0.3%, respectively.

The ICP–MS analysis was conducted at the Geochemistry Institute, SB RAS (Irkutsk), with the use of a high-resolution ELEMENT 2 mass spectrometer (ThermoQuest Finnigann MAT, Egelsbach, Germany), which provides low detection limits for the analyzed elements. Solid samples dissolved in dilute nitric acid with a concentration of about 2%. The test solution was fed by a peristaltic pump to a sprayer, in which the argon stream turned it into an aerosol. The aerosol entered the plasma through the central channel of the plasma torch, where under the influence of a high temperature (7000–8000 K), the substances contained in the sample dissociated into atoms and ionize. The resulting positively charged ions pass through the ion optics system to the analyzer, where the ions were filtered and the intensity of the ion flow was detected. The measurement accuracy was 3–5%, reproducibility for most elements corresponds to an RSD value of less than 15%.

Rb–Sr isotope studies were performed on a MI-1201-T mass spectrometer (electron optics, Sumy, Ukraine) in single-beam mode using tantalum ribbons. Rb concentrations were calculated by isotope dilution, while Sr concentrations were calculated by double isotope dilution. Sr isotope compositions were estimated without adding an indicator. The chemical treatment of samples included decomposition in a mixture of NF + $HClO_4$ (3:1) in Teflon bombs in autoclave mode at a temperature of 200 °C for 8 h. Elements were separated by the ion-exchange chromatography method with the use of Dowex resin, 50 $\times$ 8200 mesh. The error in measuring the isotope ratios did not exceed 0.05%. Reproducibility for $^{87}Rb$, $^{86}Sr$, and the $^{87}Sr/^{86}Sr$ ratio was 0.5, 0.4, and 0.03%, respectively. Blank tests for laboratory contamination showed 0.007–0.013 g/t Rb and 0.02–0.05 g/t Sr. The accuracy and reproducibility of isotope measurements were controlled by the Carbonate-70 isotope standard with an average normalized $^{87}Sr/^{86}Sr$ value of 0.7089 $\pm$ 0.0002. In the analyses, we used very high purity reagents, which were further purified if necessary.

## 3. Geological Setting

### *3.1. Tectonics of the Study Area*

The Verkhoyansk–Kolyma orogenic belt represents a collage of terranes of various affinities (e.g., [1,53–55]). The study area is located within the limits of the Polousnyi synclinorium, which forms part of the Polousnyi–Debin terrane. The terrane extends for 500 km along the north-western margin of the Kolyma–Omolon superterrane and is 50–100 km wide. The Polousnyi synclinorium is separated from the more southerly Nagondzha terrane and the Selennyakh and Ulakhan–Tas blocks of the Omulevka terrane by regional-scale thrusts. To the west, there is a thrust-faulted contact with the Kular–

Nera terrane, while the northern margin is overlain by Cenozoic deposits of the Primorsk lowland (Figure 1) [1].

The Verkhoyansk–Kolyma orogenic belt comprises several stages of tectono-magmatic evolution. The Late Jurassic–Early Cretaceous stage was marked by the closure of the Oimyakon Ocean and collision of the Siberian craton with the Kolyma–Omolon superterrane, which initiated intensive folding, faulting, and emplacement of intrusions of varying compositions, with granitoids being predominant [1,53–55]. The Late Jurassic–Early Cretaceous granitoid plutons form large arc-related belts, the Main and Northern belts, which extend along the boundary between the Kolyma–Omolon superterrane and the Verkhoyansk margin of the Siberian continent (e.g., [1,53–56]).

The post-accretionary stage (Aptian–Campanian) was characterized by the formation of numerous minor intrusions, lava fields, and subvolcanic plutons, mostly of felsic composition. The origin of these magmatic rocks is associated with the Indigirka Rift, located in the central Verkhoyansk–Kolyma orogenic belt. It is considered that the rift was formed either in relation to rifting processes in adjacent regions of the Arctic, or to extension in the back-arc region of the active paleo-Pacific continental margin [57].

The Kuranakh, Elikchan, and Istekh ore fields studied here are located within the Northern batholith belt of the north-eastern Verkhoyansk–Kolyma orogenic belt. The U–Pb ages of zircons from major plutons range from 140 to 129 Ma [56,58]. The western part of the Northern batholith belt splits into two branches flanking the Polousnyi synclinorium, within which Jurassic clastic rocks with a total thickness of up to 5 km were deposited. At the base of the section, interbedded mudstones and sandstones with endoolistostrome horizons are observed. The middle part of the section comprises siltstones and sandstones, whereas the upper part is composed of proximal turbidites grading into mudstones and siltstones, covered by andesites, basaltic andesites, and basalts. At the top of the Jurassic section, volcanic rocks of varying compositions are present, while Early Cretaceous volcanics occur in the eastern part of the synclinorium. Within the Polousnyi synclinorium, several tectonic zones with different types of folding are distinguished. The folds are characterized by a NW vergence in the central and southern zones, while they have a SE vergence in the northern zone. The boundary between these zones is delineated by the Kyun–Tas and Irgichan (Deputatsky) faults, along which ore fields with complex Sn–Au–Ag and Sn–W mineralization are found (Figure 2) [2,59].

### *3.2. Kuranakh, Elikchan, and Istekh Ore Fields*

The Kuranakh ore field includes the area of the Kuranakh massif, along with a series of rhyolite porphyry dykes and pegmatoid leucogranite or pegmatite dykes and veins, measuring several decametres long and up to 40 m thick, forming a large field in the north-western part of the massif (Figure 3) [60]. Igneous rocks of the Kuranakh massif intrude Upper Jurassic clastic rocks. The central part of the massif is composed of granodiorites, while granites are found at the periphery. The granodiorites were intruded by dykes of biotite granite with granodiorite inclusions. The rhyolite porphyry dykes are oriented mostly subparallel to NE–SW-trending faults (the Irgichan regional fault zone) (Figures 2 and 3). Dykes in the fault zones are intensely brecciated and metasomatized, along with their host granitoids. Au and Ag polymetallic occurrences are localized within these fault zones, as well as Sn, Pb, and Sb mineralization.

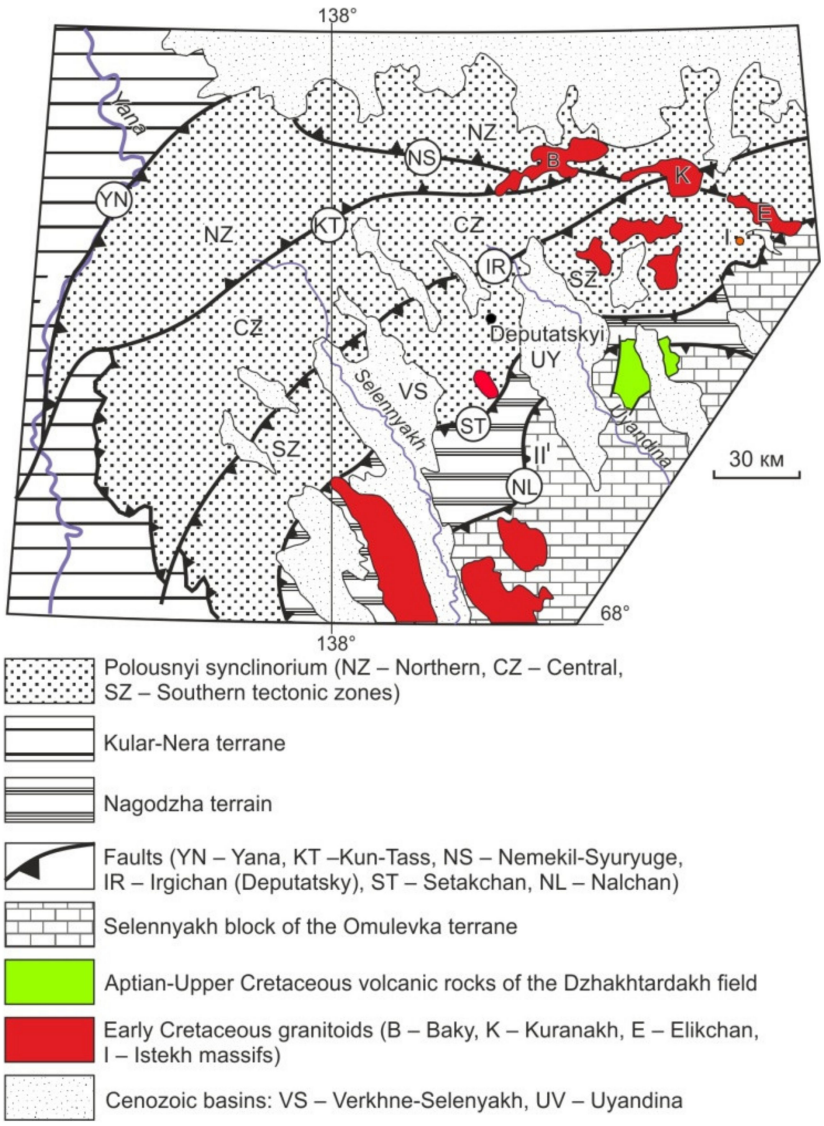


**Figure 2.** Tectonic sketch map of the Polousnyi synclinorium, modified from [59]. For location see Figure 1.

During the Berriasian–Barremian, subaerial lava flows formed low-alkali basaltic andesites, andesites, and andesitic dacites in the Elikchan ore field (Figure 4) [61]. The Aptian was characterized by the formation of a volcanic–plutonic association of rhyolites, dacites, and granitoids in the Elikchan massif. During the generation of early Albian felsic volcanic rocks, small plutons of alkaline feldspar granite and rhyolite porphyry, typically intensely greisenized, were formed. This was followed by lava flows of andesitic basalts and andesites during the Albian. The Elikchan massif forms much of the Elikchan ore field area. The north-eastern part of this massif is composed of granodiorites, with the south-western portion being composed of granites (Figure 4). The massif intrudes Jurassic clastic rocks and Berriasian–Barremian volcanic rocks, and is overlain by Aptian–Albian volcanites. In exposed sections, granites can be seen intruding earlier granodiorites. Small faults parallel to the Setakchan thrust zone (Figure 2) strike mainly NE–SW, parallel to those observed in the Kuranakh ore field, cutting the Elikchan massif and its exocontacts with the Jurassic host rocks (Figure 4). Occurrences of Sn–W and Au–Ag in fault zones are localized within the granitoids of the massif, in its exocontacts, and in intensely greisenized dykes of rhyolite and granite porphyry.

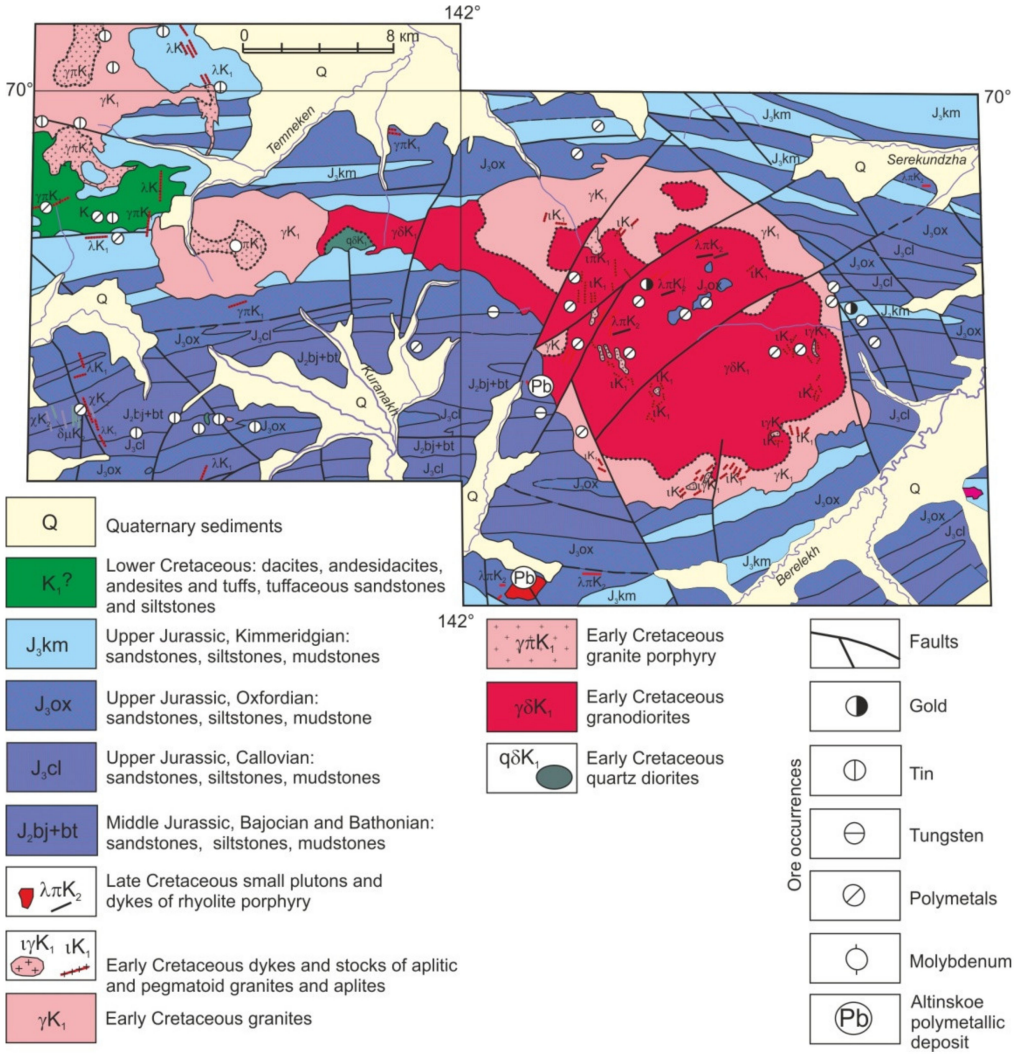


**Figure 3.** Geological map of the Kuranakh ore field, modified from [60].

The Istekh ore field comprises pre-granitoid dykes of diorite porphyry, the Istekh granitoid massif, a series of thick post-granitoid dykes of granite- and rhyolite-porphyry, and trachydolerite dykes. The Istekh massif intrudes Lower and Middle Jurassic clastic and carbonate rocks. It is slightly eroded. The western and eastern parts of the massif comprise granodiorites and granites, respectively (Figure 4). Geological mapping shows that the granites intrude the granodiorites, while granites in the apical part of the massif are greisenized. Post-granitoid rhyolite- and granite-porphyry dykes have been transformed into tourmaline–muscovite–quartz greisens. The greisenized granites and greisens are cut by numerous quartz and tourmaline–quartz veins with sulfide and fine-grained cassiterite aggregates. The Au–Ag occurrences and Istekh small ore deposit are localized in the exocontacts of the massif, while Sn–W–Au occurrences are confined to metasomatites that developed after dykes (Figure 4).

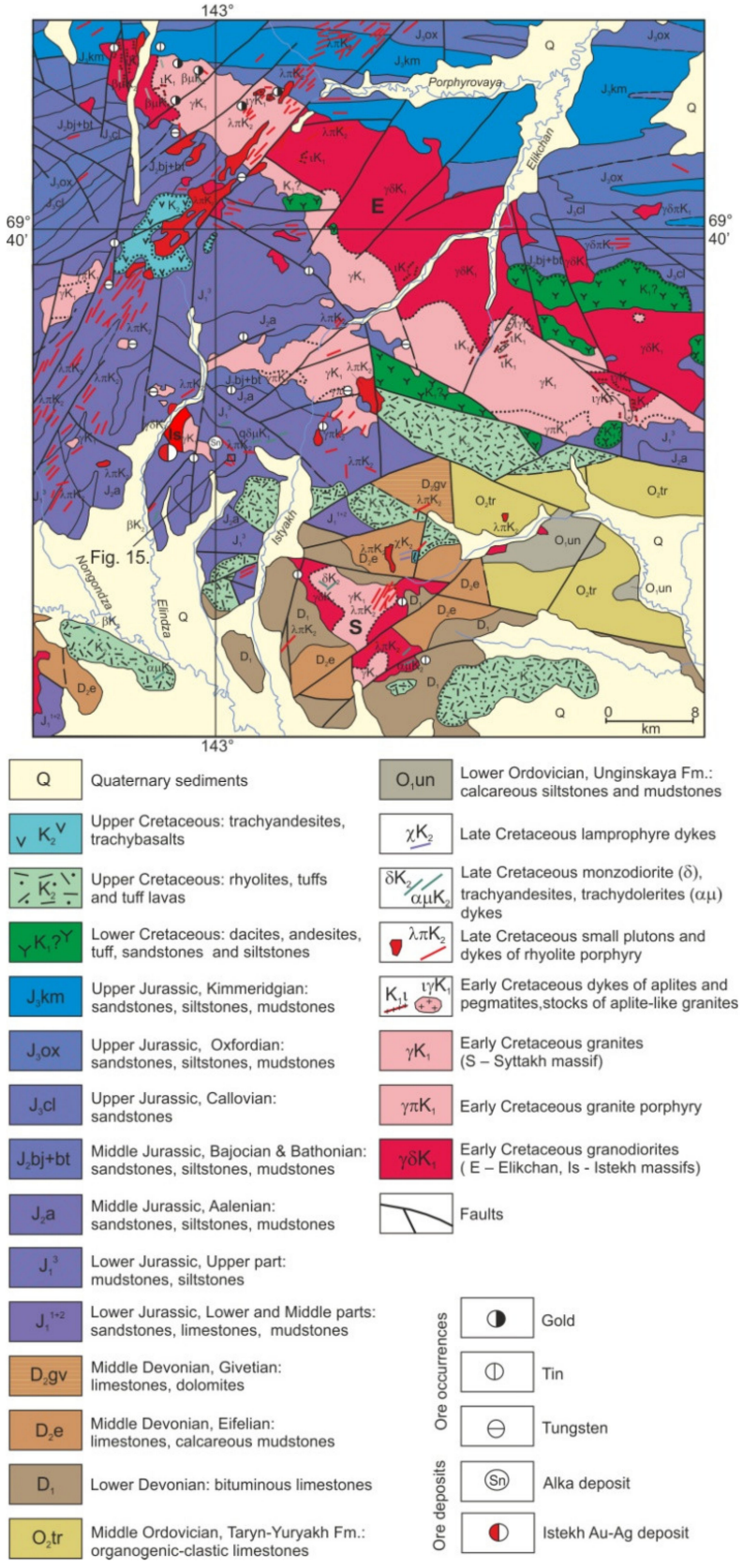


**Figure 4.** Geological map of the Elikchan and Istekh ore fields, modified from [61].

### *3.3. Geochronology of Magmatic Rocks*

During the Berriasian–Barremian, granitoid emplacement was preceded by subaerial lava flows of varying compositions, with features characteristic of active continental margin volcanic rocks [62]. An association of mainly felsic volcanic rocks and granitoids formed during the Aptian. The K–Ar isotopic age of the andesites is 140 ± 5 Ma, of the rhyodacites it is 127 ± 2 Ma, and of the rhyolites it is 120 ± 3 Ma [63]. In the Kuranakh massif, the Rb–Sr isotopic age of the granodiorites is 140 ± 2 Ma, of the amphibole–biotite granites it is 143 ± 3 Ma, of the biotite granites it is 118 ± 4 Ma, and of the pegmatites it is 116–115 Ma. In the Elikchan massif, the Rb–Sr isochron age of the granodiorites is 134 ± 2 Ma, of the biotite granites it is 122 ± 2 Ma, and of the pegmatites it is 116 ± 2 Ma. In the Istekh massif, the Rb–Sr isochron age of the granodiorites is 144 ± 9 Ma and of the biotite granites it is 114 ± 4 Ma [64]. The U–Pb (sensitive high-resolution ion microprobe) age of the granites is 129 ± 1 Ma [65]. Lava flows and dyke intrusions continued after the formation of granitoids until the Late Cretaceous. The Rb–Sr isotopic age of rhyolite- and granite-porphyry dykes is 104–102 Ma and that of trachydolerite dykes is 92–79 Ma [64]. Thus, within the studied ore fields, magmatic rocks range in age from Berriasian to Campanian.

## 4. Petrography and Mineralogy of Magmatic Rocks

As the three studied massifs share common petrographic and mineralogical features, they are discussed together. Analyses of the rock-forming minerals from granitoids of the massifs and dykes are listed in Tables S1 and S2. The rocks of the main facies of the massifs are medium-grained and have a hypidiomorphic–granular texture, which changes to nevaditic and then to porphyritic in close proximity to the chilled margin. Minerals include predominantly plagioclase and rare clinopyroxene phenocrysts, set in a fine-grained allotriomorphic groundmass of granitic composition. At endocontacts, the groundmass has a micropoikilitic texture. Granodiorites of the massifs have similar compositions (Table 1). The proportion of accessory minerals varies from 0.5% to 1.1%.

**Table 1.** Composition of granodiorites (in vol %).

| Massif | Qz | Pl | Kfs | Amp | Bt |
|---|---|---|---|---|---|
| Kuranakh | 19 | 51 | 16 | 6 | 8 |
| Elikchan | 20 | 43 | 18 | 7 | 10 |
| Istekh | 17 | 49 | 21 | 6 | 7 |

The early magmatic mineral association of granodiorites is represented by andesine labradorite and high-Ca magnesioaugite. Plagioclase forms isometric tabular crystals and aggregates, while they comprise the majority of the phenocrysts at endocontacts. Andesine (32–52% An) contains both mafic (62–67% An) and felsic (26–29% An) partially melted cores. Andesine and andesine–labradorite grains are also present, with aggregates of isometrically rounded small grains (1–3 mm) of oligoclase. We interpret such cores and aggregates as restitic.

Using the Fedorov method [37], we determined that plagioclase is characterized by multi-layer rhythmic zoning, with decreasing anorthite content from the center to the periphery of each rhythm. Each rhythm has direct zoning and is characterized by dissolution along its periphery, where there are numerous gas–liquid inclusions. The zone following dissolution is more mafic and exhibits lower structural ordering. Plagioclase from the Elikchan massif has the following composition (in An %): 43, SO 0.7 // 50, SO 0.5 → 48, SO 0.3 → 46, SO 0.6 → 44, SO 0.7 → 37, SO 0.9 → 22, SO 1.0 // 42, SO 0.6 → 44, SO 0.6 → 40, SO 0.9 → 26, SO 1 → 4, SO 0.9. Plagioclase from the Kuranakh massif has the following features: 43, SO 0.6 → 38, SO 0.7 → 40, SO 0.5 → 52, SO 0.3 // 44, SO 0.8 → 44, SO 0.6 → 36, SO 0.6 (phenocryst); 52, SO 1 → 54, SO 1 (groundmass); 36, SO 0.5 → 36, SO 0.4 → 36, SO 0.2 → 30, SO 0.4 (// = rhythm boundary, SO = structural ordering, arrow means a sequential change in the composition of plagioclase zones from the center to the

periphery of the rhythm). Thus, there is a combination of reverse zoning, which formed during magma intrusion, and direct zoning, which formed in the magma chamber. This structure of plagioclase is typical of rocks in Kuranakh and Elikchan massifs. Plagioclase grains from granodiorites of the Istekh massif are composed of a central part (52–43% An, up to 70 vol %), overgrown with narrow zones (44–36% An) and an outer rim of oligoclase composition. Thus, direct zoning of plagioclase is observed. Gas–liquid inclusions are found only at the peripheries of plagioclase grains.

Clinopyroxene forms rare short prismatic grains, as well as inclusions in the central zones of plagioclase. It is represented mainly by magnesioaugite (after the classification of [66]). The high values of the ferruginous coefficient (f) = 13.6–23.4% and $TiO_2$ contents (0.42–0.75 wt. %) suggest that the clinopyroxene corresponds to pyroxenes of highly alkaline gabbroids [67] (Table S1). The crystallization temperature of the clinopyroxene is estimated at 930–1100 °C [40,41]. In the crushed granodiorite samples, corroded grains of subcalcic magnesioaugite with a crystallization temperature of 1200–1250 °C are found (Table S1). This magnesioaugite is compositionally similar to clinopyroxenes of mafic and ultramafic rocks [67].

An amphibole replaces clinopyroxene, forming schlieren of intensely actinolitized prismatic grains. In porphyry rocks, it occupies interstitial spaces in monomineralic plagioclase aggregates. Amphibole occurs as intergrowths with large orthite grains, containing inclusions of zircon, apatite, and magnetite. It is represented mainly by magnesian hornblende, which crystallized at medium to shallow depths (0.50–2.95 kbar) under conditions of moderate to high oxygen fugacity ($-\log fO_2$ = 11.4–13.8), with a melt water content estimated at 3.2–5.3 wt. % ($H_2O$ calculated after [42] and pressure after [43], see Table S1). It is similar to amphibole in mafic rocks, with respect to proportions of ferruginosity and alkali metal contents [68]. Single relics of ferro-tschermakite, a characteristic mineral of amphibolites, are observed in hornblende schlieren.

Biotite in the granodiorites is represented by eastonite–annite with varying Fe content (Table S2) [44–48]. Biotite began to crystallize later than amphibole, penetrating into the interstices of xenomorphic and allotriomorphic quartz and K-feldspar grains. With respect to $\log(X_F/X_{OH})$–$\log(X_{Mg}/X_{Fe})$ ratios, this biotite corresponds to biotite from derivatives of crustal–mantle magmas (Figure 5) [69], and its low alumina content is comparable to biotites of highly alkaline magmatic rocks.

The biotite crystallized in an environment similar to that in which amphibole crystallized, characterized by buffer NNO, $-\log f O_2$ = 10.8–13.5, and melt water content = 3.5–5 wt. % (after [70]; Figure 6). The high oxygen, chlorine, and water fugacities during biotite crystallization are similar to those characteristic of gold-bearing ore–magmatic systems [71]. The most favorable conditions existed during the emplacement of the Istekh massif granodiorites.

The K-feldspar in the granodiorites is represented by orthoclase with a high–medium degree of structural ordering ($2V_{Np}$ = 48–62°, degree of triclinicity 0.4–0.7).

The accessory fraction of the granodiorites includes magnetite, titanite, allanite, ilmenite, chlorapatite, garnet, and zircon. Magnetite contains up to 1 wt. % and ilmenite up to 0.8 wt. % $Cr_2O_3$ values, characteristic of minerals that crystallized from basaltic or andesitic magmas [72]. The pyrope content (19–24 mol. %) in accessory garnet corresponds to a lower-crustal level of magma generation [73]. Zircon is represented by morphotypes D and J, characteristic of the derivatives of mantle or largely mantle genesis [74], in which the $ZrO_2/HfO_2$ ratio reaches typical gabbro values of 79–80 [75]. Granodiorites of all the massifs contain pyrrhotite (as inclusions in amphibole), pyrite, and impurity-rich arsenopyrite, forming small accumulations in the interstices of rock-forming minerals in association with quartz and late-generation biotite. Accessory arsenopyrite contains on average 2600 g/t Bi, 200 g/t Sn, 170 g/t Sb, 50 g/t W, and 20 g/t Ag.

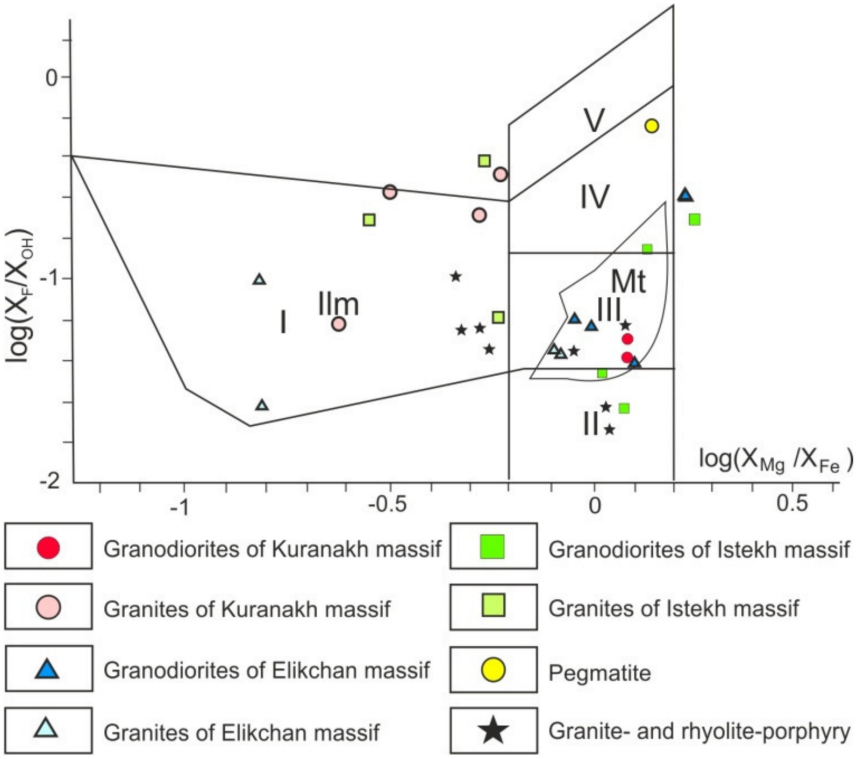


**Figure 5.** F/OH–Mg/Fe diagram for biotites of magmatic rocks. Fields of biotite derived from melts [69]: I—contaminated and assimilated marine metasediments; II—mantle; III—crust-mantle, IV—mantle-crustal, and V—crustal anatectic.

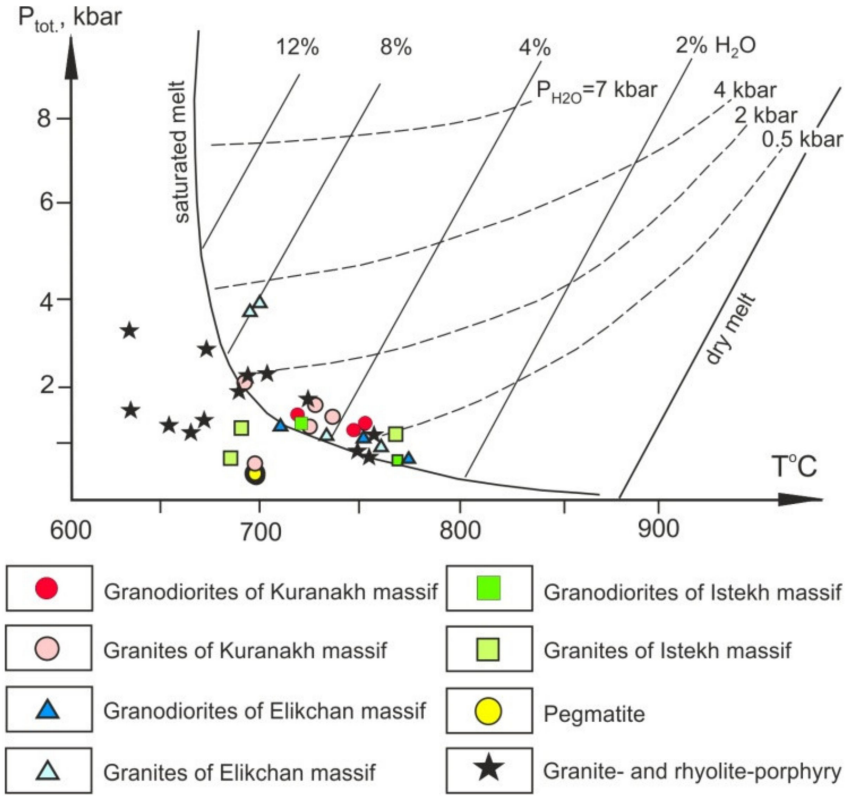


**Figure 6.** P–T-diagram of the granite-water system for independent $P_{tot.}$ and $P_{H2O}$ [70].

The granites are massive or variably textured, medium-grained, and porphyritic to nevaditic, with an allotriomorphic–granular and locally micropegmatitic groundmass. The composition of the granites is shown in Table 2.

**Table 2.** Composition of granites (in vol %).

| Massif | Qz | Pl | Kfs | Bt | Chl | Ms |
|---|---|---|---|---|---|---|
| Kuranakh | 30 | 27 | 36 | 5 | 2 | 0 |
| Elikchan | 34 | 20 | 40 | 4 | 2 | 0 |
| Istekh | 28 | 29 | 37 | 4 | 0 | 2 |

Plagioclase forms idiomorphic tabular crystals, either unzoned or directly zoned, with an intensely sericitized central part, and its composition varies from 26–32% An in phenocrysts to 12–16% An in small grains and porphyry groundmass. K-feldspar comprises medium- to low-ordered cryptoperthitic microcline ($2V_{Np}$ = 62–80°) and is typically highly albitized, but is less idiomorphic when intergrown with plagioclase. Quartz is irregular in form and occurs as intergrowths with K-feldspar. Biotite is represented by early-generation eastonite–annite, forming intergrowths with oligoclase, and by late-generation highly ferruginous siderophyllite (f = 77–87%), forming fine grains that accumulate in the interstices of salic minerals. Both generations of biotite are replaced by chlorite and muscovite. The water content of the melt ranged from 3.5 wt. % during early-generation crystallization to 8 wt. % during late-generation crystallization (see Figure 6). The pressure and temperature of biotite crystallization were obtained after [44–48] (see Table S2). Our estimates of these parameters [70] suggest that biotite crystallized under reducing conditions at moderate or low chlorine- and low fluorine-bearing fugacities. Water- and fluorine-bearing fugacities were only high during the crystallization of late-generation biotite in the granites of the Istekh massif. The water pressure did not exceed the load pressure ($P_{tot}$) (Figure 6). The biotite contains abundant monazite, ilmenite, and apatite inclusions.

The accessory fraction of the granites includes magnetite, allanite, manganiferous ilmenite, fluorapatite (0–0.42 wt. % Cl, 3.26–4.82 wt. % F, 0.2–1.2 wt. % $Y_2O_3$), zircon of S-series morphotypes characteristic of crustal granites [74], spinel, and hercynite. The rocks contain nests of radiating fibrous chlorite. During autometasomatism, muscovite aggregates developed in association with single spessartine–almandine grains (25–27 mol. % spessartine at 3.6–4 mol. % Py), arsenopyrite and chalcopyrite nests, and late-generation tourmaline grains. The granite samples also contain solitary grains of antimonite. ICP-MS analysis revealed contents of 0.02–0.1% Ag and 0.03–0.07% Sn in chalcopyrite, and 0.03–0.5% W in pyrite. The maximum content of trace elements is recorded in arsenopyrite (3.93% Bi and up to 0.2% Sb) [76].

Pegmatites and pegmatoid leucogranites of the northern part of the Kuranakh massif are medium- to coarse-grained, with pegmatitic and allotriomorphic–granular textures, respectively. They have an average composition of 30 vol % quartz, 11 vol % plagioclase, 52 vol % K-feldspar, 5 vol % biotite, and 2 vol % ore minerals. These rocks are composed of high-ordered orthoclase ($2V_{Np}$ = 50–52°), with albite perthites, low-ordered oligoclase (20–12% an, SO 0.4–0.6), quartz, and biotite. Biotite flakes in intergrowths with sulfides and titanite tend to occupy interstices in salic minerals or form monomineralic accumulations. The biotite is magnesian, with low alumina: f = 42.1%, al* = 16.2% (f = FeO/(FeO + MgO); al* = Al/(Al + Si), and is enriched in halogens. Chemical analyses indicate contents of up to 2.6 wt. % F and 1 wt. % Cl, with $Li_2O$ and $Rb_2O$ contents of 0.1 wt. % each. This biotite crystallized from a water-saturated melt at high oxygen and water fugacities and a very high halogen fugacity, the values of which are typical of highly productive ore–magmatic systems (Table S2, Figure 6). Accessory minerals include fluorapatite (2.64–5.03 wt. % F, 0.4–0.12 wt. % Cl, 0.4–0.71 wt. % $Y_2O_3$, and 0.2–0.51 wt. % $Ce_2O_3$), magnetite, titanite, allanite, native Ag and Bi, and pyrrhotite with 0.12 wt. % Bi, 0.04 wt. % Zn, 0.05 wt. % Sn, 0.025 wt. % Ag, and up to 0.4 wt. % Cr [76].

The granite and rhyolite porphyry dykes are porphyritic and glomeroporphyritic, with a microallotriomorphic and felsitic groundmass. These rocks are intensely kaolinized and sericitized. The phenocrysts are composed of quartz, sanidine ($2V_{Np}$ = 0°–34°), low-ordered albite, and low-alumina Mg–Fe biotite (Table S2). Sanidine contains drop-shaped inclusions of magnesioaugite (Table S1). Biotite phenocrysts crystallized at high oxygen, water, and chlorine fugacities (Table S2). Nests of lepidogranoblastic aggregates of quartz, fuchsite, and sulfides are observed in the groundmass. Mica is represented mainly by siderophyllite, which formed under reducing conditions from a water-saturated melt (up to 12% $H_2O$) at a water vapor pressure of up to 3 kbar. In the endocontacts of dykes, eruptive breccias can be observed in which fragments of granite porphyry and host granites are cemented by a glassy matrix of felsic composition. Granite and rhyolite porphyries are strongly brecciated and altered into sericite–kaolinite metasomatites.

Accessory minerals of rhyolite- and granite-porphyries include high-temperature magnetite with up to 8.2 wt. % $SiO_2$, a stable admixture of $Al_2O_3$ and $Cr_2O_3$ (up to 0.35 wt. %), single crystals of Cr-bearing (up to 3 wt. % Cr) native iron rich in W, Bi, Sn, and Ag, manganiferous ilmenite, titanite, allanite, zircon with up to 0.24 wt. % $U_3O_6$ and up to 0.17 wt. % $ThO_2$, and single hercynite crystals. The rocks are characterized by the presence of nests and veinlets of arsenopyrite with admixtures reaching up to 3700 g/t Pb, 330 g/t W, 200 g/t Sb, and 150 g/t Ag, as well as pyrite with 1250 g/t Zn, 230 g/t W, 150 g/t Pb, and 120 g/t Ag.

Trachydolerites are porphyritic, with phenocrysts of labradorite–bytownite, pyroxene, biotite, and less commonly, amphibole embedded in a microdoleritic or hyalopilitic matrix. The composition of pyroxene (diopside–augite) suggests it was derived from continental basaltic magmas [67]. Amphibole is represented by ferropargasite. Biotite is magnesian and crystallized in similar conditions to those characteristic of productive gold-bearing systems [71] (Table S2). In the rocks, a hyalopilitic matrix of mafic composition contains rounded and drop-like inclusions of weakly crystallized felsic glass and microgranular quartz–potassium–feldspar aggregates.

## 5. Geochemistry of Magmatic Rocks

Chemical compositions of the studied granitoids range from quartz diorites to alkali granites. Endocontacts of the Istekh massif with calcareous sandstones and siltstones of the host rock are composed of quartz monzonite (Table S3, Figure 7) [77]. The total alkalinity of the rocks increases substantially across the transition from granodiorites to granites, mainly due to an increase in potassium while the sodium content remains stable ($Na_2O/K_2O$ = 0.7–1.3 in granodiorites and 0.6–0.75 in granites). The normative composition of the rocks is similar for the three massifs.

Granodiorites are diopside–hypersthene normative, with normative albite slightly more prevalent than orthoclase and little or no normative corundum. Granites are hypersthene normative, with normative orthoclase prevailing over albite and a uniform presence of normative corundum, although in small amounts (Table 3). All rocks are metaluminous or very slightly alumina-supersaturated.

**Table 3.** Average normative composition (%) of granodiorites/granites.

| Massif | Qz | Or | Ab | An | Crn | Di | Hyp |
|---|---|---|---|---|---|---|---|
| Kuranakh | 18.3/30.7 | 22.8/29.2 | 29.7/27.4 | 15.1/9.4 | 0.1/0.3 | 1.8/0.4 | 10.1/5.6 |
| Elikchan | 20.6/32 | 23.7/29 | 26.9/27.8 | 14.9/8.1 | 0.2/1.5 | 1.2/0 | 9.8/6.1 |
| Istekh | 16.8/29.6 | 22.9/29.3 | 25.8/24 | 15.6/7.7 | 0/1.5 | 2/0 | 14.1/6.3 |

On an $Al_2O_3/(Na_2O + K_2O)$ versus $Al_2O_3/(CaO + Na_2O + K_2O)$ diagram, the granodiorites all plot within the continental arc granitoid field. However, only some granites plot within this field, while the remainder are classified as rift-related granitoids (Figure 8). In terms of composition, the granodiorites are similar to I-type granitoids from active margins, whereas the granites correspond to S-type granitoids (Figure 9).

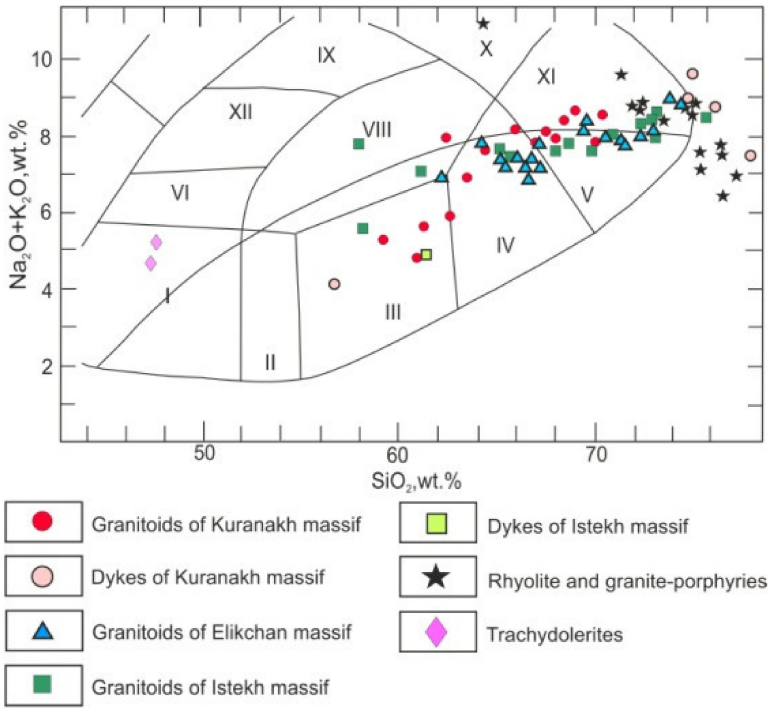


**Figure 7.** $SiO_2$–($Na_2O$ + $K_2O$) diagram for magmatic rocks. Fields on the diagram [77]: I—gabbro; II—gabbro–diorite; III—diorite, IV—granodiorite, V—granite; VI—subalkaline gabbro; VII–VIII—monzonite; IX–X—syenite; and XI—alkali granite.

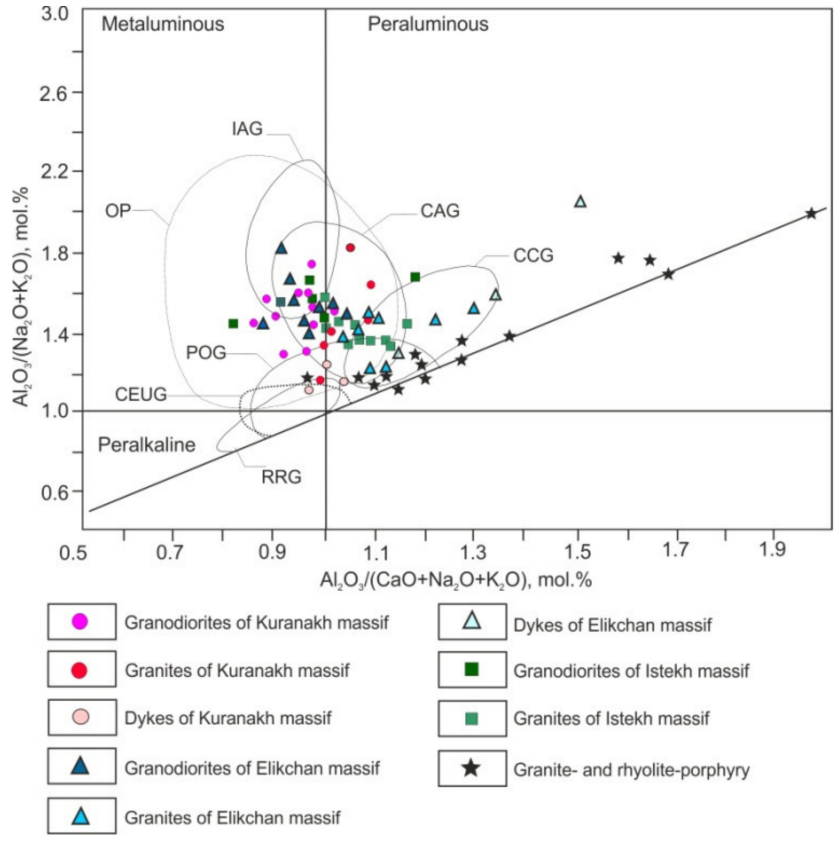


**Figure 8.** $Al_2O_3/(Na_2O + K_2O)$–$Al_2O_3/(CaO + Na_2O + K_2O)$ diagram for granitoids [78]. Granitoid fields include: IAG—island arcs; CAG—continental arcs; CCG—continental collision settings; POG—postorogenic; CEUG—continental epirogenic uplifts; and RRG—rift-related.

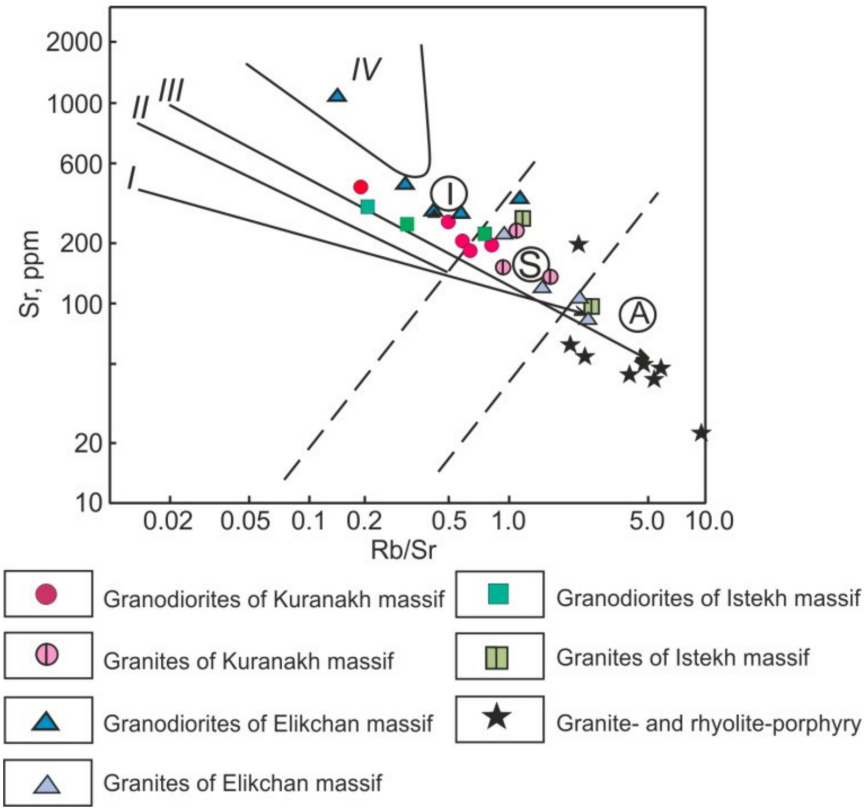


**Figure 9.** Sr–Rb/Sr diagram for granitoids. Differentiation trends of type series include [79]: I—island-arc tholeiitic; II—island-arc calcareous-alkaline; III—active margin calcareous-alkaline; IV—continental rift zones; and I, S, A—granitoid petrotypes.

The granodiorites and granites display asymmetric trends in the distribution of chondrite-normalized rare-earth elements (REEs), with significantly higher contents of light REEs (LREEs) compared to heavy REEs (HREEs) and a weak negative Eu anomaly, thus resembling magmatic formations of active continental margins. The REE patterns of the granites differ only by having a more pronounced negative Eu anomaly (Figure 10, Table S4) [51,80].

Based on the ICP–MS analysis data, the lanthanide tetrad effect of REE fractionation was calculated for a series of samples (Table S4). Two types of tetrad effect are known in natural objects: M (convex) and W (concave). The former is typical for differentiated granitoid series, whereas the latter may appear in magmatic rocks when the melt interacts with water- and halogen-rich fluids [81–83]. A tetrad effect is considered significant when its total tetrad effect (TEi) is <0.9 (W-type) and >1.1 (M-type). The tetrad effect is estimated either by the sum of the first, third, and fourth tetrads, or by the sum of the third and fourth tetrads [51,83,84]. For most of the studied samples, the total tetrad effect determined by the sum of the third and fourth tetrads is <0.9, with the lowest values observed for pegmatites.

An Al/(Mg + Fe) vs. Ca/(Mg + Fe) diagram for the studied granites indicates that their parental melt formed by selective melting of amphibolites (Figure 11) [85]. On this basis, the melt temperature is estimated at 1040–1060 °C [49]. Calculations using the alternative technique from [86] yielded similar results of 1020–1087 °C. The magma-generation pressure estimated by the value $L = (Na_2O + K_2O - 1.25)/(SiO_2 - 4.2.5)$ [87] is 1–1.1 GPa for the least differentiated granodiorite samples (L = 0.30–0.31), while the pressure calculated following the method of [88] is 1.2–1.4 GPa. The granitic melt originated from the selective melting of upper-crustal dacitic rhyolites or metagreywackes (Figure 11) at a temperature of 880–920 °C [49] or 908–972°C [86]. The pressure calculated using the above methods was 0.7–0.8 GPa (L = 0.23–0.24) [87] or 0.7–0.9 GPa [88].

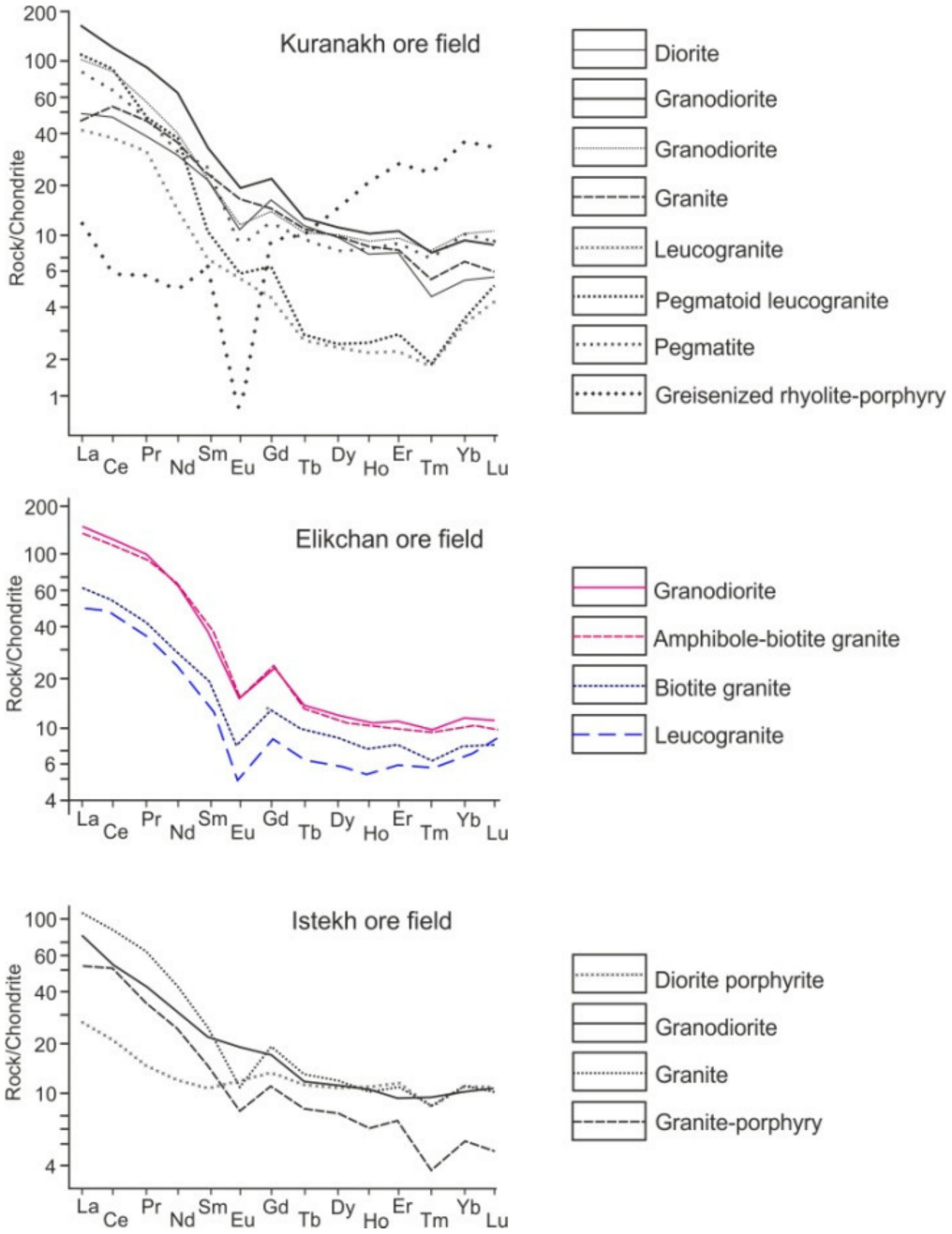


**Figure 10.** Chondrite-normalized [80] rare-earth element (REE) patterns of magmatic rocks within the Kuranakh, Elikchan, and Istekh ore fields.

Based on their composition, pegmatoid leucogranites and pegmatites of the Kuranakh massif correspond to postorogenic A-type granites (see Figures 8 and 9). The calculated magma generation conditions are similar to those for granites (P = 0.7–0.8 GPa, T = 919–935 °C), and the Y–Nb–Ce ratios correspond to a mantle or crustal–mantle protolith (Figure 12) [89].

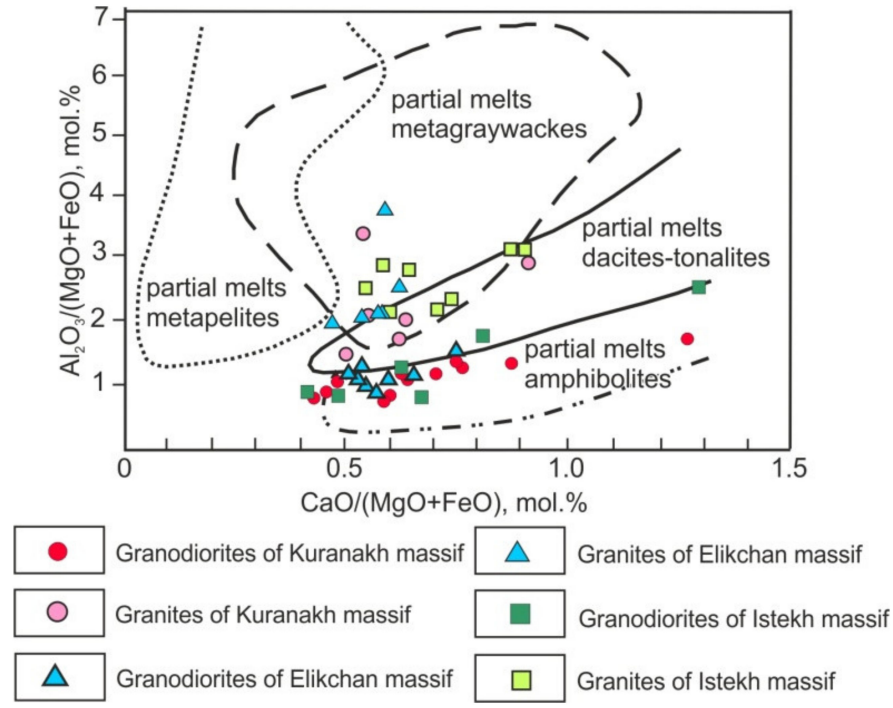


**Figure 11.** Al/(Mg + Fe) vs. Ca/(Mg + Fe) diagram for granitoids. Fields of magma-generating substrata are derived from [85].

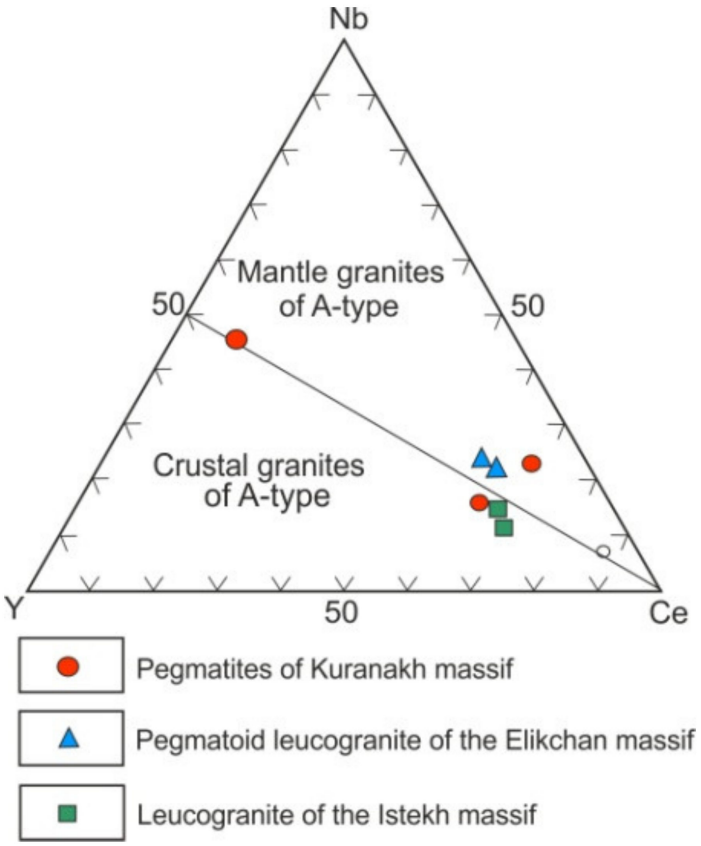


**Figure 12.** Y–Nb–Ce diagram for magmatic rocks of the Khara–Sis massif. Fields on the diagram are from [89].

Granite- and rhyolite-porphyries are highly potassic, hypersthene normative, contain a prevalence of normative orthoclase over albite, and a consistent presence of a small amount of normative corundum. In contrast to granitoids of the massifs, a higher $SiO_2$ content in granite porphyries, rhyolite porphyries, and pegmatites is accompanied by a lower ($Na_2O + K_2O$) (see Figure 7). Based on their compositional characteristics and main petrochemical coefficients, they correspond to A-type rift-related granites (Figures 8 and 9). The melt temperature determined from the least altered samples is estimated at 960–1041 °C (after [49]), which is higher than that for granites and pegmatites, while the calculated pressure (1.1–1.3 GPa) is similar to that of the granodiorites. REE distribution trends in the leucogranites and granite porphyries are similar to those in the granitoid massifs. Only the rhyolite-porphyry of the Kuranakh ore field is characterized by a sharp increase in the HREE content, which was probably caused by an intense post-magmatic change in the studied sample (Figure 10).

The trachydolerites of the dykes, the youngest magmatic rocks in the study area, are olivine-nepheline normative (13.7 mol. % Ol; 4.6 mol. % Nph; 12.4% mol. Or) and belong to the shoshonite alkaline series. The calculated pressure is 3 GPa [90] and the temperature is 1160 °C [50].

The trace element distribution in granitoids of the massifs and in dykes is highly irregular. However, all of the studied magmatic rocks, regardless of age and composition, exhibit a well-defined geochemical specialization for chalcophile elements (Sb, Bi, Ag, and As), W and B. These elements are characteristically derived from latitic magma (Table S5) [52]. High Ba and Sr contents, along with La/Yb values of 10–46, also indicate a latitic geochemical affinity [91,92]. On a Ce/Yb–Ta/Yb diagram [93], granitoid data plot in the shoshonite series field, although a single diorite porphyrite data point plots in the calc-alkaline series field (Figure 13).

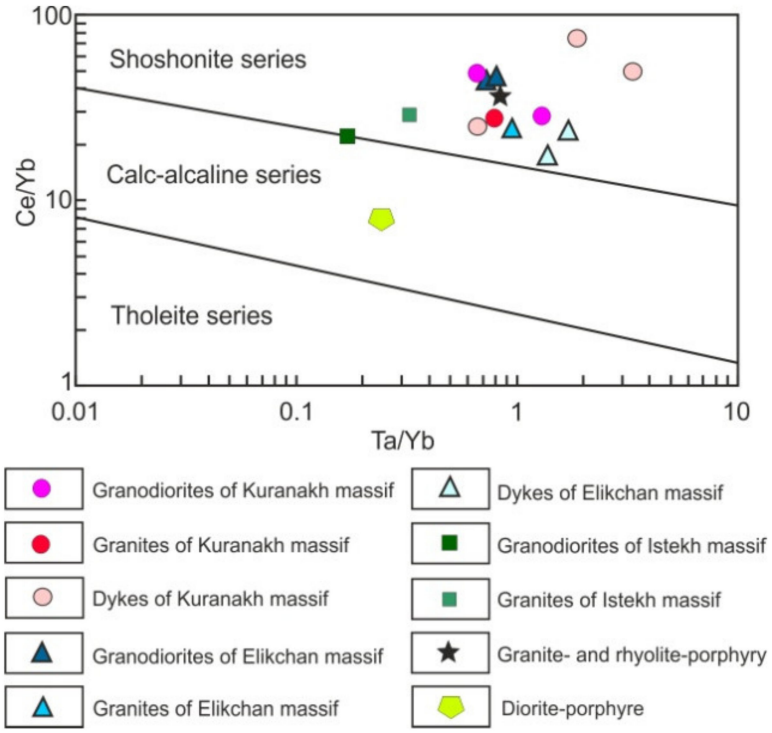


**Figure 13.** Ce/Yb vs. Ta/Yb diagram. Field definitions are derived from [93].

The highest Au contents are present in granitoids of the Kuranakh massif (Table S5). However, only small Au–Ag occurrences are found in the Kuranakh and Ekikchan massifs, along with their exocontacts. On the other hand, in the south-western exocontact of the

Istekh massif, the Alka deposit (Figure 4) contains up to 1 kg/t of Ag, up to 10 g/t of Au, and accompanying Sb, Sn, Pb, Zn, Cu, and Bi mineralization.

Biotite granites contain higher contents of Li, B, and Sn relative to the granodiorites. These granites crystallized in reducing conditions at a slightly higher fluorine fugacity than is characteristic for granodiorites, under conditions similar to those of rare-metal systems.

Pegmatites and leucogranites of the Kuranakh massif contain the highest Ag, Au, Sn, Mo, As, Zn, Pb, Cu, and Sb contents compared to the other granitoids, with Ag content in hand specimens of up to 0.5 kg/t.

Abundant Sn, Mo, W, and As are typical of the rhyolite- and granite-porphyry dykes. The main volatile component is B, while Li and Rb contents are at Clarke levels and F is slightly higher than the Clarke value. However, the distribution patterns of Li, Rb, F, Ba, and Sr in these rocks correspond to magmatic systems with a high rare-metal potential (Figure 14) [94].

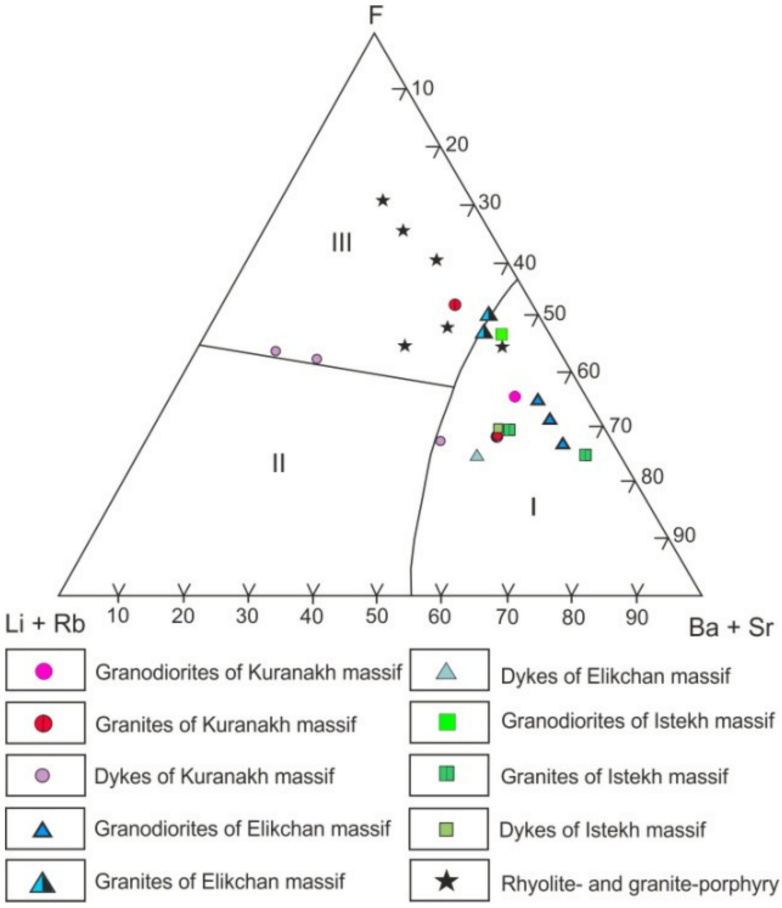


**Figure 14.** (Li + Rb)–F–(Ba + Sr) diagram for granitoids. Fields on the diagram are derived from [94]: I—barren; II—weakly mineralized; and III—highly mineralized granitoids.

Dykes and clastic host rocks are cut by numerous quartz and tourmaline–quartz veins with nests of sulfides, cassiterite, and wolframite. Sn–W mineralization is confined to the most intensely reworked dykes, which have been transformed into quartz–kaolinite–muscovite greisens containing an average of 0.5% F and 300 g/t of Sn (sometimes up to tenths of %). A significant supply of volatiles took place into the host rocks, with the water content reaching 3.8–6.2 wt. % and the F content reaching 0.23–0.4% at a distance of 200 m from the contact.

Trachydolerite dykes are latitic in terms of their trace element content and distribution. They are enriched in the same elements as the granitoids of the massifs and the dyke rocks (Table S5). Tourmalinization and Sn–W mineralization are not superimposed on the

trachydolerites. In the Istekh ore field, greisenized rhyolite porphyry dykes are cut by fault zones, hosting tourmaline–quartz veins containing 0.1–1.5 wt. % Sn, 0.5 wt. % W, and 0.1–1.0 g/t of Au. These faults and veins are cross-cut by a trachydolerite dyke (Figure 15). Thus, the age of the Sn, W, and Au mineralization here is post-granitic and post-rhyolitic, but pre-dates intrusion by trachydolerite dykes. The younger quartz–carbonate–chlorite and chlorite veins, which contain large fragments of greisenized granite porphyry, intrude the trachydolerites.

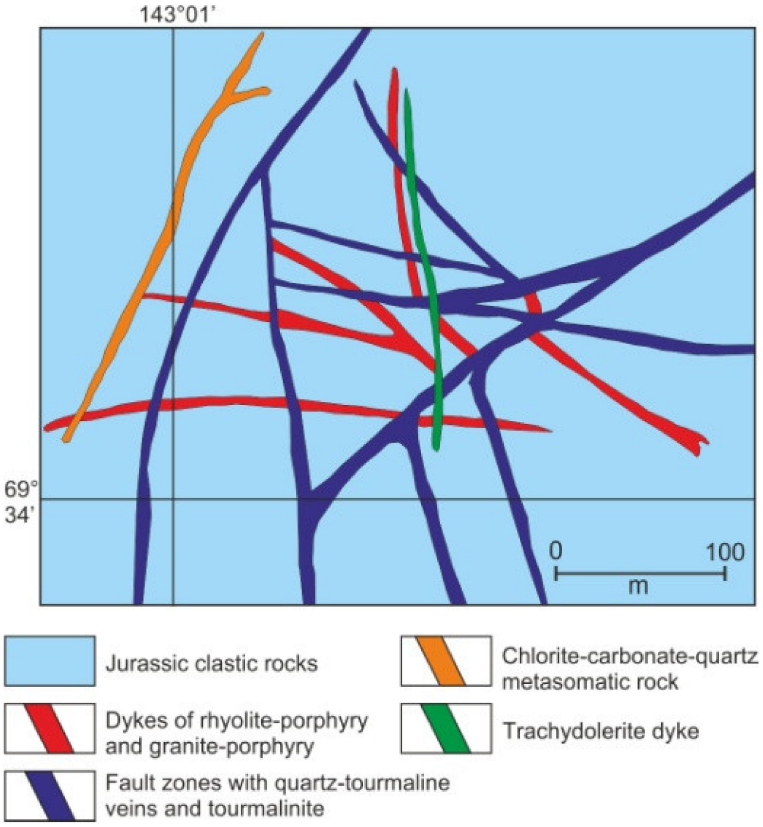


**Figure 15.** Field geological map of the south-eastern part of the Istekh ore field (compiled by V.A. Trunilina). See Figure 4 for location.

During the post-magmatic stage, both granitoids and trachydolerites were propylitized along fault zones, which increased the Pb, Sb, As, Ag, and Au contents by up to 100 times those observed at distance from these zones, while Sn, Mo, and B contents showed lesser increases. Occurrences of Au in low-sulfide ores are confined to these zones of propylitization. The propylitized rocks are cut by siderite veins containing galena and cassiterite, as well as monomineralic galena veins bearing Ag and Sb sulphosalts. Therefore, these processes formed the Sn–Ag–Sb mineralization, superimposed on trachydolerite dykes, which concluded the ore–magmatic evolution in the study area. The Altinsky deposit formed at the intersections of faults with the Kuranakh massif, in which metasomatites are intensely enriched in Ag (up to 12%), Pb (up to 61%), As (0.6%), Bi (0.5%), and Sb (0.3%), and also contain insignificant admixtures of Au, Cu, Sn, and W.

## 6. Discussion

The magmatic and metallogenic evolution of the studied part of the Northern batholith belt and case-study ore fields included several stages (Figure 16).

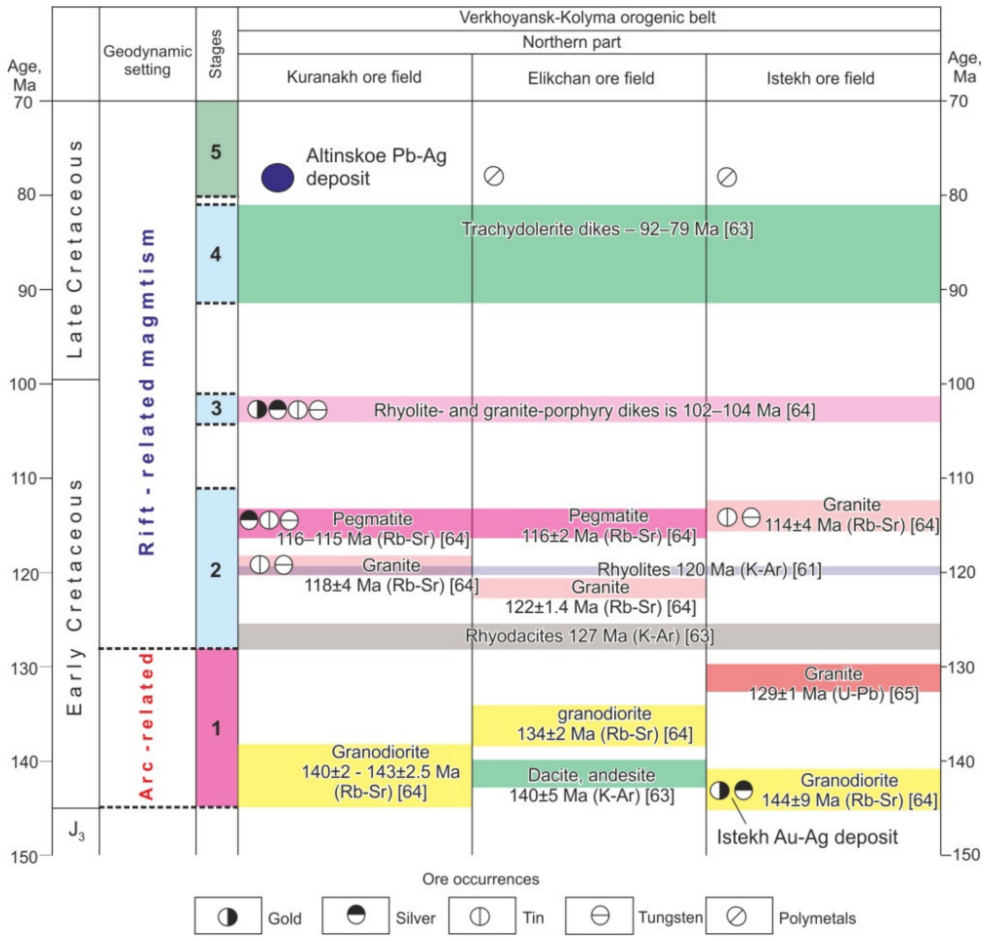


**Figure 16.** Magmatic, metallogenic and tectonic events in the northern Verkhoyansk–Kolyma orogenic belt, correlated on the basis of isotopic ages.

The first stage (Berriasian–Barremian) was marked by the formation of volcanogenic arc-related basalts–andesites–rhyolites [62], along with the emplacement of granodiorites with characteristics similar to those of granitoids from active margins (Figures 8 and 9). This stage was related to closure of the Oimyakon Ocean and collision of the Siberian craton with the Kolyma–Omolon superterrane [1,53–55].

The parental melt, which formed the granodiorites, was generated by the selective melting of amphibolites (Figure 11), with estimated temperatures of 1020–1087 °C. Based on thermodynamic calculations, Bogatikov [95] and Ryabchikov [96] showed that conductive heat flows in the lithosphere weakened during the course of the Phanerozoic. As a result, granite could not form in the crust without an additional heating source to instigate the ascent of mantle melts into lower-crustal horizons. According to [97], the inflow of asthenospheric heat can initiate extensive crustal melting and form Sn-bearing granites. Isotopic studies [17,98] have demonstrated a significant contribution of the mantle for the generation of crustal granites with W–Sn mineralization in Amazonia and China.

As shown above, the geochemical features of the rocks correspond to those of granitoids from the latitic series (see Tables S4 and S5; Figure 13). It is generally considered that rocks of the shoshonite–latite series are genetically related to the mixing and mingling of mantle-level fluid-saturated mafic melts with crustal substrata [91,99–101]. For the studied magmatic rocks, this interpretation is also supported by the specific compositions of clinopyroxenes and biotites, which are comparable to those derived from mafic melts and crustal-mantle melts, respectively (Figure 5). These are characterized by high $Cr_2O_3$ contents in accessory magnetites and ilmenites, and by the prevalence of D and J morphotypes among accessory zircons. A similar mixing mechanism for mantle and crustal

granitic melts has been proposed for the well-studied North Bohemian massif [102] and the Qianlishan granites of south-east China [103]. This mantle–crust interaction may also account for the low $^{87}Sr/^{86}Sr$ values observed in the granodiorites (0.7079 and 0.7067 for the Kuranakh and Elikchan massifs, respectively).

The formation of small gold occurrences and the Istekh Au–Ag deposit is related to the first stage of magmatic and metallogenic evolution in the study area. Volatiles played a key role in the origin of gold ore occurrences. Sulfide complexes, $CO_2$-rich fluids, and saline fluids are considered as the transporting agents of gold [3,24,25,104]. According to McCoy [104], saline fluids separate from the melt during early crystallization stages, whereas those saturated in $CO_2$ separate during later stages. The importance of chlorine as an active transporter of gold in magmatogenic fluids of Au-bearing granitoid systems has been noted in numerous studies (e.g., [71,104–106]), including in a study of gas–liquid inclusions in minerals of auriferous granitoids in north-east Asia [29].

Granodiorite crystallization in all of the investigated massifs occurred under conditions of high oxygen, water, and chlorine fugacities (Table S2), which are known to promote Au mineralization [66]. However, the structure of plagioclase grains from granodiorites of the Kuranakh and Elikchan massifs, characterized by abundant gas–liquid inclusions at the peripheries of rhythms and an inferred temperature increase at the beginning of each rhythm (a decrease in the degree of structural ordering), indicates a multi-stage magmatic evolution, with repeated residence in intermediate magma chambers where crystallization was accompanied by a partial degassing of the melt. Partial degassing was due to decreasing temperature and pressure in these intermediate chambers, which led to reduced Cl solubility [107,108]. Accordingly, as the melt ascended to the surface with residence in intermediate chambers, it became depleted in chlorine. As a result, the Au-transporting capacity of fluids was reduced, which may explain why only small Au occurrences formed in association with granitoids of the Elikchan and Kuranakh massifs.

Plagioclase grains from granodiorites of the Istekh massif are characterized by direct zoning. Gas–liquid inclusions are present only at the peripheries of grains. Biotite crystallized under maximum $H_2O$ (Log f $H_2O$ = 3.00–3.54) and Cl (Log f HCl = 2.91–4.73) fugacities (Table S2). These conditions, favoring the formation of ore-bearing hydrothermal solutions, were realized in the development of the Istekh Au–Ag deposit, with mineralization also being favored by a lack of time spent in intermediate chambers during magma ascent. Correlations of Au content with trace elements of the iron group, such as Co, Ni, V, and Cr (correlation coefficient r = 0.46–0.99) on the one hand, and with boron (r = 0.47) on the other hand, indicate a polygenetic source of Au. High correlations of Au content with Ag, Bi, Pb, and Cu (r up to 0.77) reflect the complex nature of the deposit [109].

The second stage of magmatic and metallogenic evolution (Aptian–early Albian) (Figure 16) was represented by the formation of granites, leucogranites, and pegmatites. Compositionally, the granites are intermediate between active margin granitoids and rift-related granitoids, whereas the leucogranites correspond to rift-related rocks. Granitic melts were derived from upper-crustal dacite–tonalite or metagraywacke substrata (Figure 11). The composition of their constituent rock-forming and accessory minerals (including the F/OH–Mg/Fe ratio of biotites; Figure 5), the manganous character of ilmenites, the prevalence of zircon crystals of morphotype S, and $^{87}Sr/^{86}Sr$ values of 0.7110–7112 are suggestive of a crustal origin for the rocks. Geochemically, the granites are similar to S-type granites (Figure 9). In a discrimination diagram for granite types [110] (Figure 17), data for the granodiorites and granites define opposite trends, suggesting the independent development of their magma chambers and confirming the polygenetic nature of the massifs. A polygenetic nature is further supported by the lack of common trends in the Nb/Ta and Zr/Hf ratios between the massifs, which are widely regarded as good indicators for the occurrence of crystallization differentiation [111,112]. A decrease in the Zr/Hf ratio from granodiorites to granites is observed only for rocks from the Elikchan massif. This ratio increase in rocks from the Kuranakh massif, whereas it is essentially uniform for rocks

from the Istekh massif. The Nb/Ta ratio decreases in rocks from the Istekh and Elikchan massifs but increases in rocks from the Kuranakh massif (Table S4).

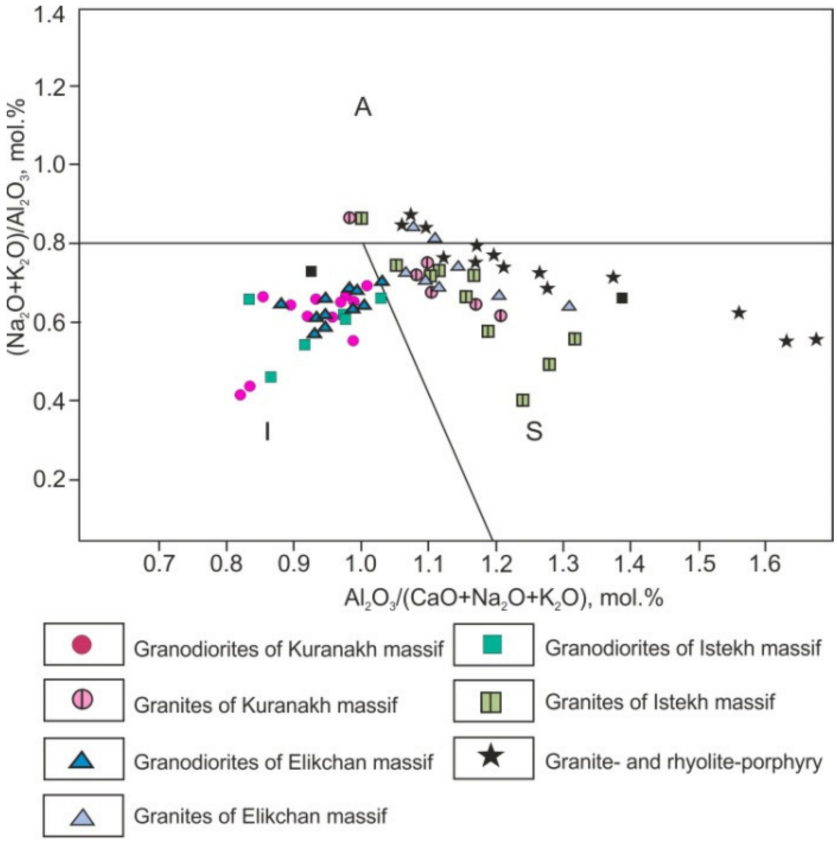


**Figure 17.** $(Na_2O + K_2O)/Al_2O_3$–$Al_2O_3/(CaO + Na_2O + K_2O)$ diagram for granitoids. Fields on the diagram are derived from [110].

Biotite granites crystallized in reducing conditions, with higher levels of F fugacity compared to those observed for granodiorites, suggesting that these granites are close to rare-metal systems. However, the water pressure in the system was lower than $P_{tot}$ (Figure 6), suggesting that these granites are accompanied only by impregnated cassiterite, wolframite, molybdenum, and Ag- and Bi-bearing sulfides, despite the well-defined geochemical specialization in Sn, W, Mo, and Ag.

Pegmatoid leucogranites and pegmatites of the Kuranakh massif intrude the biotite granites. The calculated temperatures and pressures of magma generation are similar to those for the granites. However, unlike the granites, they crystallized under conditions of high oxygen, water, and halogen fugacity (Table S2). They are also distinguished by a high crystallization temperature, the presence of orthoclase rather than microcline, a magnesian composition of biotite, and a low alumina content. Their Y–Nb–Ce ratios correspond to a mantle or crustal-mantle protolith (Figure 12). These characteristics preclude an interpretation of these rocks as late low-temperature differentiates of a granite chamber. Rather, they must be derived from an independent melt formed from crustal substrata under the influence of an additional deep-seated source of heat and fluids, or from the lower horizons of granite chambers reinvigorated by this additional heat and fluid source. Their crystallization at anomalously high water and halogen fugacities, along with their high Sn, Ag, Au, As, Pb, and Sb contents, make these leucogranites and pegmatites promising targets for prospective complex mineralization.

The third stage of magmatic and metallogenic evolution (Albian) was characterized by rift-related felsic lava flows and thick (up to 200 m) rhyolite- and granite-porphyry dykes (Figure 16). Melt generation took place at a higher temperature compared to the

granites and pegmatites, but at a similar pressure to the granodiorites (1.3 GPa). The rocks are characterized by the early magmatic paragenesis of high-Ca augite with sanidine and moderately ferruginous biotite, which indicates the high alkalinity of the melts, as well as by the presence of titanomagnetite among the accessory minerals with high $SiO_2$, $Al_2O_3$, and $Cr_2O_3$ contents and solitary grains of Cr-bearing native iron. These features suggest that the rocks were most likely derived from a melt that originated from post-orogenic re-melting of lower-crustal substrata with the continued input of additional heat from a deep-seated source and, possibly, partial mixing of mafic and silicic melts.

The presence of eruptive breccias in the selvages of some rhyolite- and granite-porphyry bodies indicates that the fluid pressure far exceeded the external pressure during crystallization, which may explain the high ore content. These magmatic systems produce abundant rare-metal mineralization (Figure 14). Crystallization of these rocks from parent melts began at high water and chlorine fugacities, which may account for the presence of Au–Ag ores where these rocks are distributed. Further crystallization occurred at high water and boron fugacities, as indicated by the transformation of the host rocks into tourmaline-bearing exogreisens and tourmalinites. The Sn–W mineralization is localized in metasomatites that formed after dykes. A sharp increase in B and F contents, both in metasomatites developed after rhyolite- and granite-porphyries and in the host rocks, must be related to the supply of volatiles from an external, probably deep-seated, source.

The fourth stage of magmatic and metallogenic evolution (Turonian–Campanian) was characterized by the eruption of subalkaline and alkaline basalts with features common to rift-related volcanics [62], and by the intrusion of latitic trachydolerite dykes (Figure 16). The olivine–nepheline-normative composition, calculated conditions of magma generation, and La/Yb–Yb ratios (1.35–13.3) suggest that the trachydolerite dykes crystallized from melts generated in metasomatically enriched mantle [113]. The presence of xenogenic quartz, amphibolite xenoliths, quartz–K-feldspar liquation aggregates, and rhyolitic globules are indicative of the contamination of mantle melt by crustal material, along with limited syntexis of basaltic and rhyolitic melts.

The trachydolerites are rich in Sn, As, Sb, Pb, Bi, Au, and W, comparable to magmatic rocks of the three previous stages, and their B, Sn, Pb, and Bi contents are much higher than the corresponding Clarke values.

During the fifth post-magmatic stage (Maastrichtian–Paleogene?), granitoids were propylitized with the supply of Pb, Sb, As, Ag, Sn, Mo, and B along fault zones, while SnS–Ag–Sb occurrences and the Altinsky Ag-polymetallic deposit were formed (Figure 6). This mineralization was superimposed on rhyolite-porphyry, granite-porphyry, and trachydolerite dykes, representing the completion of the ore–magmatic cycle of the study area.

The first stage of magmatism and metallogeny in the study area occurred in an active continental margin setting, during the closure of the Oimyakon Ocean and collision of the Kolyma–Omolon superterrane with the Siberian continental margin (e.g., [1,53–55]). We interpret the second to fifth stages as occurring during crustal extension and continental rifting in the central Verkhoyansk–Kolyma orogenic belt (e.g., [1,53–57]) (Figure 16).

The high calculated temperatures of the granitoid melts, which increased from granites to pegmatites and rhyolite- and granite-porphyries, the high-temperature character of pegmatite, and the presence of Cr-bearing native iron in rhyolite- and granite-porphyries and of rhyolite globules in trachydolerites, indicate mantle–crust interaction during the evolution of magmatism in the study area. Together with the latitic trend in the distribution of trace elements, these features suggest that mafic–ultramafic magma chambers were present in the study area throughout the Cretaceous.

The calculated tetrad effects, the common geochemical specialization of all magmatic rocks of the study area, and the estimated P–T conditions of magma generation together suggest an intensive interaction of granitoid melts with fluid flow. The possibility of such a process is supported by the results of a He and Ar isotope systems study on ore-bearing granitoids from China, which indicated that ore-forming fluids there comprised a mixture of crustal fluid with mantle components [98]. The maximum concentrations of Li, Rb, B,

and F in trachydolerites, relative to Clarke values and the other studied igneous rocks, suggest that the magmatic melt was one of the sources of these solutions and at least partly of the ore elements.

## 7. Conclusions

1 The relationships established between igneous rocks of varying compositions and the available geological data enabled the recognition of five stages in the magmatic and metallogenic evolution of the Kuranakh, Elikchan, and Istekh ore fields in the north-eastern Verkhoyansk–Kolyma orogenic belt, Eastern Russia. The first stage (Berriasian–Barremian) was marked by the generation of arc-related volcanic rocks and the emplacement of granodiorites in an active continental margin geodynamic setting. The Au–Ag occurrences of the Istekh ore field were formed during this stage. The second to fourth stages occurred in a rifting environment. During the second stage (Aptian–early Albian), granites containing cassiterite, wolframite, and molybdenite were emplaced. Granites and pegmatites of the Kuranakh massif exhibit Ag, Sn, Au, As, Pb, and Sb mineralization, while granites of the Istekh ore field have associated Sn and W occurrences. The third stage (Albian) was characterized by the accumulation of felsic volcanic rocks and intrusion of rhyolite- and granite-porphyry dykes. These magmatic rocks are accompanied by Au–Ag and Sn–W mineralization. The fourth stage (Turonian–Campanian) featured the production of subalkaline basaltoids and the intrusion of trachydolerite dykes rich in volatiles and ore elements. During the fifth (post-magmatic) stage, magmatic rocks located along the fault zones were propylitized with the formation of Sn–S–Ag–Sb ores and the Altinsky Pb–Ag deposit;

2 The studied granitoid massifs are polygenetic. Parental melts for the granodiorites were derived from amphibolite substrata, whereas those for the granites were derived from dacites–rhyolites or metagreywacke substrata. The rhyolite and granite porphyries were most likely derived from melt that originated from post-orogenic re-melting of lower-crustal substrata with the continued input of additional heat from a deep-seated source. The trachydolerites crystallized from melts of metasomatized mantle. The rhyolite porphyries and trachydolerites exhibit evidence of syntexis of basaltic and rhyolitic melts;

3 Compositions of the rock-forming and accessory minerals of the studied magmatic rocks, the high calculated temperatures of magma generation, the geochemically anomalous characteristics of pegmatites, and the common geochemical characteristics of the magmatic rocks reflect their location in a long-lived and highly permeable zone of the lithosphere, which allowed additional heat, volatiles, and ore elements to be supplied from subcrustal sources to magma-generation levels during the magmatic evolution of the study area.

**Supplementary Materials:** The following are available online at https://www.mdpi.com/2075-163X/11/3/266/s1, Table S1: Contents of major (wt. %) elements in pyroxenes and amphiboles of magmatic rocks of Kuranakh, Elikchan, and Istekh ore fields, Table S2: Contents of major (wt. %) elements in biotites of magmatic rocks of Kuranakh, Elikchan, and Istekh ore fields, Table S3: Contents of major (wt. %) elements in magmatic rocks of Kuranakh, Elikchan, and Istekh ore fields, Table S4: Contents of trace and rare elements in magmatic rocks (ppm) (ICP-MS) and parameters of tetrad effects, Table S5: Geochemical composition of the magmatic rocks.

**Author Contributions:** Conceptualization, V.A.T.; Methodology, V.A.T.; Investigation, V.A.T. and A.V.P.; Writing-Original Draft Preparation, V.A.T.; Writing–Review & Editing, A.V.P. All authors have read and agreed to the published version of the manuscript.

**Funding:** Field and analytical works are partly supported by project of the DPMGI SB RAS. Magmatic and metallogenic investigations and interpretation were funded by the Russian Science Foundation grant 20-17-00169.

**Institutional Review Board Statement:** Not applicable.

**Informed Consent Statement:** Not applicable.

**Data Availability Statement:** Not applicable.

**Acknowledgments:** The author expresses gratitude to all who performed analytical research. Special thanks are due to S.P. Roev for his help in preparing the graphic material for the article. We thank three anonymous reviewers for their constructive comments, suggestions, and corrections, which very much helped to improve the manuscript. We are grateful to James Barnet for correcting the English.

**Conflicts of Interest:** The authors declare no conflict of interest.

## References

1. Parfenov, L.M.; Kuz'min, M.I. (Eds.) *Tectonics, Geodynamics and Metallogeny of the Sakha Republic (Yakutia)*; MAIK Nauka/Inteperiodica: Moscow, Russia, 2001. (In Russian)
2. Prokopiev, A.V.; Borisenko, A.S.; Gamyanin, G.N.; Pavlova, G.G.; Fridovsky, V.Y.; Kondrat'eva, L.A.; Anisimova, G.S.; Trunilina, V.A.; Ivanov, A.I.; Travin, A.V.; et al. Age constraints and tectonic settings of metallogenic and magmatic events in the Verkhoyansk-Kolyma folded area. *Russ. Geol. Geophys.* **2018**, *59*, 1237–1253. [CrossRef]
3. Thompson, J.F.H.; Sillitoe, R.H.; Baker, T.; Laug, J.R.; Mortenson, J.K. Intrusion-related gold deposits associated with tungsten-tin provinces. *Mineral. Depos.* **1999**, *34*, 323–324. [CrossRef]
4. Flerov, B.L. *Tin Deposits of the Yana-Kolyma Fold Region*; Nauka: Novosibirsk, Russia, 1976. (In Russian)
5. Mitrofanov, N.P. *Geodynamic Conditions for the Formation of Tin Deposits in the North-Western Sector of the Pacific Ore Belt*; VIMS: Moscow, Russia, 2013; Volume 29. (In Russian)
6. Fershtater, G.B. *Petrology of Major Intrusive Associations*; Nauka: Moscow, Russia, 1987. (In Russian)
7. Tischendorf, G.; Palchen, W. Zur klassification von Granitoides. *Z. Geol. Wiss. Berlin.* **1985**, *13*, 615–627. (In German)
8. Frost, B.R.; Arculus, R.J. A geochemical classification for granitic rocks. *J. Petrol.* **2001**, *42*, 2033–2048. [CrossRef]
9. Barbarin, B.A. Review of the relationships between granitoid types, their origins and their geodynamic environments. *Lithos* **1999**, *46*, 605–626. [CrossRef]
10. Zhou, X.M.; Li, W.X. Origin of Late Mesozoic rocks in southeastern China: Implications for lithospheric subduction and underplating of mafic magmas. *Tectonophysics* **2000**, *326*, 269–287. [CrossRef]
11. Chen, G.N.; Grapes, R. *Granite Genesis: In Situ Melting and Crustal Evolution*; Springer: Berlin, Germany, 2007.
12. Shcheglov, A.D.; Govorov, I.N. *Nonlinear Metallogeny*; Nedra: Leningrad, Russia, 1987. (In Russan)
13. Gonevchuk, G.A.; Gonevchuk, V.G. The heterogeneous and polychronous Chalba granite pluton in the Komsomolsk ore district in the Far East of Russia with regard to new conceptions of the geological structure of the region. *Russ. J. Pac. Geol.* **2013**, *7*, 369–383. [CrossRef]
14. Nekrasov, I.Y. *Tin in Magmatic and Postmagmatic Processes*; Nauka: Moscow, Russia, 1984. (In Russian)
15. Trunilina, V.A.; Orlov, Y.S.; Roev, S.P. *Geology and Ore Content of Magmatites of the Polousnyi Ridge*; YSC SB RAS publishing house: Yakutsk, Russia, 1996. (In Russian)
16. Kamber, B.S.; Ewart, A.; Collerson, K.D.; Bruce, M.C.; Mc Donald, G.D. Fluid–mobile trace element constraints on the role of slab melting and implications for Archaean crustal growth models. *Contrib. Mineral. Petrol.* **2002**, *144*, 38–56. [CrossRef]
17. Lenharo, S.L.R.; Pollard, P.J.; Born, H. Petrology and textural evolution of granites associated with tin and rare-metals mineralization at the Pitinga mine, Amazonas, Brazil. *Lithos* **2003**, *66*, 37–64. [CrossRef]
18. Kozlov, V.D. Trace-element composition and origin of granitoids from the Shakhtama complex and Kukul'bei rare-metal complex (Aga zone, Transbaikalia). *Russ. Geol. Geophys.* **2011**, *5*, 526–536. [CrossRef]
19. Efremov, S.V. *Rare-Metal Granitoids of Chukotka: Geochemistry, Sources of Matter, and Model of Formation*; Synopsis of Doctoral Thesis in Geology and Mineralogy: Irkutsk, Russia, 2012. (In Russian)
20. Schuiling, R.D. Tin belts on the continents around the Atlantic ocean. *Econ. Geol.* **1967**, *62*, 540–551. [CrossRef]
21. Shcheglov, A.D. Tin deposits and the mantle. *Glob. Tecton. Metallog.* **1991**, *4*, 69–74. [CrossRef]
22. Dias, G.; Simões, P.P.; Ferreira, N.; Leterrierc, J. Mantle and Crustal Sources in the Genesis of Late-Hercynian Granitoids (NW Portugal). Geochemical and Sr-Nd Isotopic Constraints. *Gondwana Res.* **2002**, *5*, 287–305. [CrossRef]
23. Safonov, Y.G. Gold and gold-bearing deposits of the World: Genesis and metallogenic potential. *Geol. Ore Depos.* **2003**, *45*, 265–278.
24. Groves, D.I.; Condie, K.C.; Goldfarb, R.J.; Hronsky, J.M.A.; Vielreicher, R. Secular changes in global tectonic processes and their influence on the temporal distribution of gold-bearing mineral deposits. *Econ. Geol.* **2005**, *100*, 203–224. [CrossRef]
25. Goldfarb, R.; Taylor, R.D.; Collins, G.S.; Goryachev, N.A.; Orlandini, O.F. Phanerozoic continental growth and gold metallogeny of Asia. *Gondwana Res.* **2014**, *25*, 49–102. [CrossRef]
26. Goryachev, N.A.; Pirajno, F. Gold deposits and gold metallogeny of Far East Russia. *Ore Geol. Rev.* **2014**, *59*, 123–151. [CrossRef]
27. Goryachev, N.A. Gold deposits in the Earth's history. *Geol. Ore Depos.* **2019**, *61*, 495–511. [CrossRef]
28. Khanchuk, A.I. *Geodynamics, Magmatism, and Metallogeny of Eastern Russia*; Dal'nauka: Vladivostok, Russia, 2006. (In Russian)
29. Gamyanin, G.N.; Goryachev, N.A.; Bakharev, A.G.; Kolesnichenko, P.P.; Zaitsev, A.I.; Diman, E.N.; Berdnikov, N.V. *Conditions of Initiation and Evolution of Granitoid Gold-Ore-Magmatic Systems in Mesozoides of Northeast Asia*; SVKNII DVO RAN: Magadan, Russia, 2003; ISBN 5-94729-048-0. (In Russian)

30. Borisenko, A.S.; Zhmodik, S.M.; Naumov, E.A.; Spiridonov, A.M.; Berzina, A.N. Age limits of formation of gold mineralization in Eastern Transbaikalia. In *Materials of the Conference Native Gold: Typomorphism of Mineral Associations, Conditions for the Formation of Deposits, Problems of Applied Research*; IGEM RAS: Moscow, Russia, 2010; pp. 82–83. (In Russian)
31. Dril, S.I.; Gerasimov, N.S.; Sasim, S.A.; Vladimirova, T.A.; Spiridonov, A.M.; Il'ina, N.N.; Chukanova, V.S. Pb isotope evolution of some model gold-ore and polymetallic deposits of the Mongol-Okhotsk foldbelt. In *Modern Problems of Geochemistry. Transactions of the 33rd All-Russian Meeting Devoted to 95th Anniversary of Academician, L.V. Tauson*; Institute of Geography, SB RAS: Irkutsk, Russia, 2012; Volume 2, pp. 218–220. (In Russian)
32. Abramov, B.N. Sources for ore-bearing fluids at Au, Mo, W, and Pb-Zn deposits in eastern Transbaikalia (from rare and REE distribution data). *Izv. Tomsk Polytech. Univ. Engeneering Georesources* **2019**, *330*, 71–83. (In Russian) [CrossRef]
33. Borisenko, A.S.; Spiridonov, A.M.; Isokh, A.E.; Prokopiev, A.V.; Lebedev, V.I.; Gas'kov, I.V.; Zorina, L.D.; Kostin, A.V.; Naumov, E.A.; Tretyakova, I.G. Highly productive stages of mafic and granitoid magmatism in North Asia, assessment of their potential resources, scientific substantiation of criteria for prediction and search for large deposits (Cu-Ni-Pt, Co, Au, Ag, and rare-metal). *Probl. Mirageny Russ. Spec. Issue Electron. J. Vestnic ONZ RAS* **2012**, 237–252. (In Russian) [CrossRef]
34. Janoušek, V.; Farrow, C.M.; Erban, V. Interpretation of whole-rock geochemical data in igneous geochemistry: Introducing Geochemical Data Toolkit (GCDkit). *J. Petrol.* **2006**, *47*, 1255–1259. [CrossRef]
35. Carr, M.J. *Igpet for Windows*; Terra Softa Inc.: Somerset, NJ, USA, 2010.
36. Korinevsky, E.V. PetroExplorer-a new computer program for storing and calculating chemical analyses of minerals and rocks. In *Abstracts of the VI International School of Earth Sciences Named after L. L. Perchuk*; Institute of mineralogy UB RAS: Odessa, Ukraina, 2010; pp. 63–66. (In Russian)
37. Kile, D.E.; The Universal Stage: The Past, Present, and Future of a Mineralogical Research Instrument. *Geochem. News.* **2009**, *140*. Available online: http://www.geochemsoc.org/publications/geochemicalnews/gn140jul09/theuniversalstage.htm (accessed on 10 June 2009).
38. Saranchina, G.M.; Kozhevnikova, V.N. *Fedorovsky Method: Determination of Minerals, Microstructural Analysis*; Nedra: Leningrad, Russia, 1985. (In Russian)
39. Baraz, V.R.; Levchenko, V.P.; Povzner, A.A. *Structure and Physical Properties of Crystals*; Ural State University: Yekaterinburg, Russia, 2009. (In Russian)
40. Lindsley, D.H. Pyroxene thermometry. *Am. Mineral.* **1963**, *68*, 477–493.
41. Yavuz, F. Win Pyrox: A Windows program for pyroxene calculation classification and thermobarometry. *Am. Mineral.* **2013**, *98*, 1338–1359. [CrossRef]
42. Rudolfi, R.; Renzolli, A. Calcic amphiboles in calc-alkaline and alkaline magmas: Thermobarometric and chemometric empirical equations valid up to 1130 °C and 2.2 Gpa. *Contrib. Mineral. Petrol.* **2012**, *163*, 877–895. [CrossRef]
43. Hammerstrom, J.M.; Zen, E. Aluminium in Hbl an empirical igneous. *Am. Mineral.* **1986**, *71*, 1297–1313.
44. Uchida, E.; Endo, S.; Makino, M. Relationship between solidification depth of granitic rocks anf formation of hydrothermal ore deposits. *Resour. Geol.* **2007**, *57*, 47–56. [CrossRef]
45. Henry, D.J.; Guidotti, C.V.; Thompson, J. The Ti-saturation surface for low-to-medium pressure metapelitic biotites: Implication for geothermometry and Ti-substitution mechanismus. *Am. Mineral.* **2005**, *90*, 316–328. [CrossRef]
46. Troshin, Y.P.; Grebenschikova, V.I.; Antonov, A.Y. Volatile components in biotites and metallogenic specialization of intrusions. In *Mineralogical Criteria for Ore Content Assessment*; Nauka: Leningrad, Russia, 1981; pp. 73–83. (In Russian)
47. Wones, D.R.; Eugster, H.P. Stability of biotite: Experiment, theory and application. *Am. Mineral.* **1965**, *9*, 1228–1272.
48. Tindle, A.G.; Webb, P.C. Estimation of lithium contents in trioctahedral micas using microprobe data: Application to micas from granitic rocks. *Eur. J. Mineral.* **1990**, *2*, 595–610. [CrossRef]
49. Jung, S.; Pfander, J.A. Source composition and melting temperatures of orogenic granitoids–constrains from $CaO/Na_2O$, $Al_2O_3/TiO_2$ and accessory mineral saturation thermometry. *Eur. J. Mineral.* **2007**, *1*, 5–40. [CrossRef]
50. French, W.J.; Cameron, E.P. Calculation on the temperature of crystallization of silicates from basaltic melts. *Mineral. Mag.* **1981**, *44*, 19–26. [CrossRef]
51. Irber, W. The lanthanide tetrad effect and its correlation with K/Rb, Eu/Eu*, Sr/Eu, Y/Ho, and Zr/Hf of evolving peraluminious granite suites. *Geochem. Cosmochem. Acta* **1999**, *63*, 489–508. [CrossRef]
52. Ovchinnikov, L.N. *Applied Geochemistry*; Nedra: Moscow, Russia, 1990. (In Russian)
53. Nokleberg, W.J.; Parfenov, L.M.; Monger, J.W.H.; Norton, I.O.; Khanchuk, A.I.; Stone, D.B.; Scotese, C.R.; Scholl, D.W.; Fujita, K. *Phanerozoic Tectonic Evolution of the Circum-North Pacific. Professional Paper 1626*; U.S. Geological Survey: Reston, VA, USA, 2000.
54. Nokleberg, W.J. (Ed.) *Metallogenesis and Tectonics of Northeast Asia. Professional Paper 1765*; U.S. Geological Survey: Reston, VA, USA, 2010.
55. Toro, J.; Miller, E.; Prokopiev, A.V.; Zhang, X.; Veselovskiy, R.V. Mesozoic orogens of the Arctic from Novaya Zemlya to Alaska. *J. Geol. Soc.* **2016**, *173*, 989–1006. [CrossRef]
56. Akinin, V.V.; Miller, E.L.; Toro, J.; Prokopiev, A.V.; Gottlieb, E.S.; Pearcey, S.; Polzunenkov, G.O.; Trunilina, V.A. Episodicity and the dance of late Mesozoic magmatism and deformation along the northern circum-Pacific margin: North-eastern Russia to the Cordillera. *Earth Sci. Rev.* **2020**, *208*, 103272. [CrossRef]
57. Trunilina, V.A.; Parfenov, L.M. Indigirka belt of extension Earth crust. In *Tectonics, Geodynamics, and Metallogeny of the Sakha Republic (Yakutia)*; Parfenov, L.M., Kuzmin, M.I., Eds.; Nauka/Interperiodika: Moscow, Russia, 2001; pp. 277–290. (In Russian)

58. Layer, P.W.; Newberry, R.; Fujita, K.; Parfenov, L.M.; Trunilina, V.A.; Bakharev, A.G. Tectonic setting of the plutonic belts of Yakutia, Northeast Russia, based on $^{40}Ar/^{39}Ar$ and trace element geochemistry. *Geology* **2001**, *29*, 167–170. [CrossRef]
59. Oxman, V.S.; Prokopiev, A.V. Terrigenous tectonic melanges of the Polousnyi synclinorium. *Otechestvennaya Geol.* **2000**, *5*, 47–50. (In Russian)
60. Musalitin, L.A. *Geologic Map of the Russia Scale 1:200 000, Sheet R-54-XXI, XXII. Explanatory Note*; Nedra: Moscow, Russia, 1967. (In Russian)
61. Boyarshinov, V.V. *Geological Map of the Russia, Scale 1: 200 000, Sheet R-54-XXIII, XXIV. Explanatory Note*; Nedra: Moscow, Russia, 1968. (In Russian)
62. Trunilina, V.A.; Roev, S.P.; Orlov, Y.S. *Volcanic-Plutonic Belts of North-East Yakutia*; Sakhapoligrafizdat: Yakutsk, Russia, 2007; 152p. (In Russian)
63. Nenashev, N.I.; Zaitsev, A.I. *Evolution of Mesozoic Granitoid Magmatism of the Yana-Kolyma Fold Area*; YaF SO AN SSSR: Yakutsk, Russia, 1985. (In Russian)
64. Trunilina, V.A.; Roev, S.P.; Orlov, Y.A. *Granitoids of the Batholitic Belts in the Northeastern Verkhoyansk-Kolyma Mesozoides*; Media-Holding "Yakutia": Yakutsk, Russia, 2013. (In Russian)
65. Gertseva, M.V.; Sysoev, I.V. Stages of formation of Main Kolyma plutonic belt. In *Fundamental Problems of Tectonics and Geodynamics. V.1*; GEOS: Moscow, Russia, 2020; pp. 165–170. (In Russian)
66. Rock, N.M.S. The International Mineralogical Association (IMA/CNMMN) pyroxene nomenclature scheme: Computerization and its consequences. *Mineral. Petrol.* **1990**, *43*, 99–119. [CrossRef]
67. Ryabov, V.V.; Zolotukhin, V.V. *Minerals of Differentiated Traps*; Nauka: Novosibirsk, Russia, 1977. (In Russian)
68. Hollister, L.S.; Grissom, G.C.; Peters, E.K.; Stowell, H.H.; Sisson, V.B. Confirmation of the empirical correlation on the Al in hornblende with pressure of solidification of calc-alkaline plutons. *Am. Mineral.* **1987**, *72*, 231–239.
69. Brimhall, G.H.; Crerar, D.A. Ore fluids: Magmatic to supergene. In *Termodynamic Modeling of Geological Materials. Minerals, Fluids and Melts*; De Gruyter: Berlin, Germany, 1987; Volume 17, pp. 235–321.
70. Brown, G.G. A comment on the role of water in the partial fusions of crystal rocks. *Earth Planet. Sci. Lett.* **1970**, *9*, 355–358. [CrossRef]
71. Förster, H.J. Halogen Fugicities (HF, HCl) in Melts and Fluids. A. Surv. of Published Data. *Z. Geol. Wiss.* **1990**, *18*, 255–266.
72. Rub, M.G.; Ashikhmina, N.A.; Gladkov, N.I. Typomorphic features of accessory minerals and their significance for identification of genesis and ore content of granitoids. In *Granitoids of Folded and Activated Regions and Their Ore Content*; Nauka: Moscow, Russia, 1977; pp. 197–235. (In Russian)
73. Ermolov, P.V.; Izoh, A.E.; Vladimirov, A.G. Garnet as an indicator of the conditions of granite formation in the crust. *DAN Russia* **1979**, *246*, 208–211. (In Russian)
74. Pupin, J.P. Zircon and Granite Petrology. *Contrib. Mineral. Petrol.* **1980**, *73*, 207–220. [CrossRef]
75. Lyakhovich, V.V. *Accessory Minerals of Rocks*; Nedra: Moscow, Russia, 1979. (In Russian)
76. Trunilina, V.A.; Orlov, Y.S.; Roev, S.P. Composition and genetic aspects of the formation of granitoids of the latite series of the Polousnyi ridge (north batholith zone of the Verkhoyansk-Kolyma mesozoides. *Pacif. Geol.* **2002**, *5*, 15–27. (In Russian)
77. Wilson, M. *Igneous Petrogenesis*; Unwin Hayman: London, UK, 1989.
78. Maniar, P.D.; Piccoli, P.M. Tectonic discrimination of granitoids. *Geol. Soc. Am. Bull.* **1989**, *101*, 635–643. [CrossRef]
79. Datsenko, V.M. Petrogeochemical typification of granitoids of the south-western framing of the Siberian platform. In *Materials of the Second All-Russian Petrographic Meeting*; Komi SC UB RAS: Syktyvkar, Russia, 2000; Volume 2, pp. 270–274. (In Russian)
80. Hofmann, A.W. Mantle geochemistry: The message from oceanic volcanism. *Nature* **1997**, *385*, 219–228. [CrossRef]
81. Kawabe, I. Tetrad effects and fine structures of REE abundance patterns of granitic and rhyolitic rocks. *Geochem. J.* **1995**, *29*, 213–230. [CrossRef]
82. Zhenhua, Z.; Xiaolin, X.; Xiaodong, H.; Yixian, W.; Qiang, W.; Zhiwei, B.; Jahn, B. Controls on the REE tetrad effect in granites:Evidence from the Qianlishan and Baerzhe Granites, China. *Geochem. J.* **2002**, *36*, 527–543.
83. Gusev, A.I.; Gusev, A.A. Tetrad effect of fractionation of rare earth elements and its use in solving problems of granitoids petrology. *Achiev. Mod. Nat. Sci.* **2011**, *5*, 45–49. (In Russian)
84. Nakamura, K.; Morishita, T.; Chang, Q.; Neo, N.; Kumagai, H. Discovery of lanthanide tetrad effect in an oceanic plagiogranite from an Ocean Core Complex at the Central Indian Ridge 25°S. *Geochem. J.* **2007**, *41*, 135–140. [CrossRef]
85. Gerdes, A.; Worner, G.; Henk, A. Post-collisional granite generation and HT-LP metamorphism by radiogenic heating: The Variscan South Bohemian Batholith. *Geol. Soc.* **2000**, *157*, 577–587. [CrossRef]
86. Rainer, V. The Abschatzung der Bildungs temperature magmatischer Schmeltzen. *Z. Geol. Wissen.* **1998**, *18*, 5–14.
87. Piskunov, B.M.; Abdurakhmanova, A.I.; Kim, C.U. Composition-depth ratio for volcanoes of the Kuril island arc and its petrological significance. *Volcanol. Seismol.* **1979**, *4*, 57–67. (In Russian)
88. Belyaev, G.M.; Rudnik, V.A. *Formational-Genetic Types of Granitoids*; Nedra: Leningrad, Russia, 1978. (In Russian)
89. Eby, N. Chemical subdivision of the A-type granitoids: Petrogenetic and tectonic implications. *Geology* **1992**, *20*, 641–644. [CrossRef]
90. Perchuk, L.L.; Aranovich, L.A.; Kosyakova, N.A. A. Thermodynamic models of the origin and evolution of basalt magmas. *Vestn. MSU Ser. Geol.* **1982**, *4*, 3–26. (In Russian)
91. Towson, L.V.; Gundobin, G.M.; Zorina, L.D. *Geochemical Fields of Ore-Magmatic Systems*; Nauka: Novosibirsk, Russia, 1987. (In Russian)

92. Turner, S.; Arnaud, N.; Liu, J.; Rogers, N.; Hawkesworth, C.; Harris, N.; Kelley, S.; Van Calsteren, P.; Deng, W. Post-collision, shoshonitic volcanism on the Tibetan Plateau: Implications for Convective Thinning of the Lithosphere and the Source of Ocean Island Basalts. *J. Petrol.* **1996**, *37*, 45–71. [CrossRef]
93. Pearce, J.A.; Harris, N.B.W.; Tindle, A.G. Trace element discrimination diagrams for the tectonic interpretation of the granitic rocks. *J.Petrol.* **1984**, *25*, 956–963. [CrossRef]
94. Kozlov, V.D. *Geochemistry and Ore Content of Granitoids of Rare Metal Provinces*; Nauka: Novosibirsk, Russia, 1985. (In Russian)
95. Bogatikov, O.A.; Tsvetkov, A.A. *Magmatic Evolution of Island Arcs*; Nauka: Moscow, Russia, 1988. (In Russian)
96. Ryabchikov, I.V. Physical and chemical conditions of the processes of generation and differentiation of acid and medium magmas. In *Igneous Rocks. Acid and Medium Rocks*; Nauka: Moscow, Russia, 1987; pp. 348–358. (In Russian)
97. Pohl, W.L.; Birubarema, M.; Lehman, B. Neoproterozoic rare metal (Sn, Ta, W) and gold metallogeny of the Central Africa Region. *Appl. Earth Sci. Trans. Inst. Min. Metall. B* **2013**, *122*, 66–82. [CrossRef]
98. Hu, R.-Z.; Bi, X.-W.; Jiang, G.-H.; Chen, H.-W.; Peng, J.-T.; Qi, Y.-Q.; Wu, L.-Y.; Wei, W.-F. Mantle-derived noble gases in ore-forming fluids of the granite-related Yaogangxian tungsten deposit, Southeastern China. *Mineral. Depos.* **2012**, *47*, 623–632. [CrossRef]
99. Antipin, V.S. *Geochemical Evolution of Calc-Alkaline and Subalkaline Magmatism*; Nauka: Novosibirsk, Russia, 1992. (In Russian)
100. Volynets, A.O.; Churikova, T.G.; Wörner, G.; Gordeychik, G.N.; Layer, P. Quaternary volcanic rocks in the Kamchatka back arc region: Implications for subduction geometry and slab history at the Pacific–Aleutian junction. *Contrib. Mineral. Petrol.* **2010**, *159*, 659–687. [CrossRef]
101. Sasim, S.A.; Dril, S.I.; Travin, A.V.; Vladimirova, T.A.; Gerasimov, N.S.; Noskova, Y.V. Shoshonite-latite series of the Eastern Transbaikalia: $^{40}Ar/^{39}Ar$ age, geochemistry, and Sr-Nd isotope composition of rocks from the Akatui volcano-plutonic association of the Aleksandrovskii Zavod depression. *Russ. Geol. Geophys.* **2016**, *57*, 756–772. [CrossRef]
102. Siebel, W.; Trzebski, R.; Stettner, G.; Hecht, L.; Casten, U.; Hohndorf, H.; Muller, P. Granitoid magmatism of the NW Bohemian massif revealed: Gravity data, composition, age relations and phase concept. *Geol. Rundsch.* **1997**, *86*, 45–63. [CrossRef]
103. Jiang, Y.H.; Jiang, S.Y.; Zhao, K.D.; Ling, H.F. Petrogenesis of Late Jurassic Qianlishan granites and mafic dykes, Southeast China: Implications for a back-arc extension setting. *Geol. Mag.* **2006**, *143*, 457–474. [CrossRef]
104. McCoy, D.T.; Newberry, R.J.; Layer, P.W.; Di Marchi, J.J.; Bakke, A.A.; Masterman, J.S.; Minehane, D.L. Plutonic-related gold deposits of interior Alaska. *Econ. Geol. Monogr.* **1997**, *9*, 191–241.
105. Diman, E.N.; Nekrasov, I.Y. High-temperature solubility of gold in water and genesis of gold-ore deposits. *Izv. Vuzov Geol. Razved.* **1987**, *11*, 66–74. (In Russian)
106. Borisenko, A.S.; Gas'kov, I.N.; Dashkevich, E.G.; Okrugin, A.M.; Ponomarchuk, A.V.; Travin, A.V. Geochronology of magmatic processes and ore-formation in the Central Aldan gold-ore region. In *Abstracts of the Intern. Symp. Large Igneous Provinces of Asia*; Institute of Earth Crust SB RAS: Irkutsk, Russia, 2011; pp. 38–39.
107. Webster, J.D.; Goldoff, B.; Vetere, F.; Botcharnikov, R.E.; McBirney, A.; Doherty, A. Experimental and modeled chlorine solubilities in aluminosilicate melts at 1 to 7000 bars and 700 to 1250 °C: Applications to magmas of Augustine Volcano, Alaska. *Am. Mineral.* **2015**, *100*, 522–535. [CrossRef]
108. Chevychelov, V.Y. Partitioning of Volatile Components (Cl, F, and $CO_2$) in water-Saturated Fluid–Magma Systems of Various Composition. *Petrology* **2019**, *6*, 585–605. [CrossRef]
109. Trunilina, V.A.; Orlov, Y.S.; Babushkina, S.A. Latite ore-bearing magmatic systems of the North-east of the Verkhoyansk-Kolyma mesozoids. In *Ore Deposits of the Continental Margins*; Gonevchuk, G.A., Fatyanov, I.I., Eds.; Dalnauka: Vladivostok, Russia, 2001; Volume 2, pp. 22–38. (In Russian)
110. Maeda, J. Opening of the Kuril Basin deduced from the magmatic history of Central Hokkaido, northern Japan. *Tectonophysics* **1990**, *174*, 235–255. [CrossRef]
111. Zaraisky, G.P.; Aksyuk, A.M.; Devyatova, V.N.; Udoratina, O.V.; Chevychelov, V.Y. Zr/Hf ratio as an indicator of fractionation of rare-metal granites by the example of the Kukulbei complex. *Eastern Transbaikalia. Petrology* **2008**, *16*, 710–736. [CrossRef]
112. Breiter, K.; Müller, A.; Leichmann, J.; Gabašova, A. Textural and chemical evolution of a fractionated granitic system: The Podlesí stock, Czech Republic. *Lithos* **2005**, *80*, 323–345. [CrossRef]
113. Drill, S.I.; Kuzmin, M.I.; Tsipukova, S.S.; Zonenshain, L.P. Geochemistry of basalts from the West Woodlark, Lau and Manus basins: Implication for their petrogenesis and source rock composition. *Mar. Geol.* **1997**, *142*, 57–83. [CrossRef]